Evidence of a Transient Ozone Depletion Event in the Early Hunga Plume Above the Indian Ocean

Tristan Millet [1], Hassan Bencherif [1], Thierry Portafaix [1], Nelson Bègue [1], Alexandre Baron [2], Valentin Duflot [1,*], Cathy Clerbaux [3,4], Pierre-François Coheur [4], Andrea Pazmino [3], Michaël Sicard [1,5], Jean-Marc Metzger [6], Guillaume Payen [6], Nicolas Marquestaut [6], and Sophie Godin-Beekmann [3]

[1]LACy, Laboratoire de l'Atmosphère et des Cyclones (UMR 8105 CNRS, Université de La Réunion, Météo-France) Saint-Denis de La Réunion, France
[2]Cooperative Institute for Research in Environmental Sciences, and NOAA Chemical Sciences Laboratory, Boulder, USA
[3]LATMOS/IPSL, Sorbonne Université, UVSQ, CNRS, Paris, France
[4]Spectroscopy, Quantum Chemistry and Atmospheric Remote Sensing, Université Libre de Bruxelles (ULB), Brussels, Belgium
[5]CommSensLab-UPC, Universitat Politècnica de Catalunya, Barcelona, Spain
[6]Observatoire des Sciences de l'Univers de La Réunion (OSUR), CNRS/Université de La Réunion/Météo-France, UAR 3365, Saint-Denis, France
[*]now at : Department for Atmospheric and Climate Research, NILU – Norwegian Institute for Air Research, Kjeller, Norway

Correspondence: Tristan Millet (tristan.millet@univ-reunion.fr)

Abstract. On 15 January 2022, the Hunga volcano (20.5° S, 175.4° E) erupted, releasing significant amounts of water vapor (H_2O) and a moderate quantity of sulfur dioxide (SO_2) into the stratosphere. Due to the general stratospheric circulation of the southern hemisphere, this volcanic plume traveled westward and impacted the Indian Ocean and Reunion (21.1° S, 55.5° E) a few days after the eruption. This study aims to describe observations of a transient ozone depletion event in the first week following the eruption. The Ozone Mapping and Profiler Suite Limb Profiler (OMPS-LP) aerosol extinction profiles were used to investigate the vertical and latitudinal extension of the volcanic plume over the Indian Ocean. The volcanic aerosol plume was also observed with an aerosol lidar and a sun-photometer located at Reunion. The impact of this plume on stratospheric ozone was then investigated using the Microwave Limb Sounder (MLS) and Infrared Atmospheric Sounding Interferometer (IASI) ozone profiles. Results show that the volcanic plume was observed over Reunion at altitudes ranging from 26.8 to 29.7 km and spanned more than 30 degrees of longitude and 20 degrees of latitude on 21 January. IASI ozone maps on this date reveal clear stratospheric ozone depletion, with maximum Total Column Ozone (TCO) and Stratospheric Column Ozone (SCO) anomalies of -40.1 ± 4.8 DU and -49.9 ± 4.7 DU, respectively. Hunga-influenced MLS profiles reveal 1σ significant ozone anomalies at distinct pressure ranges, directly related to the locations of the water vapor anomalies and sulfate aerosol clouds.

1 Introduction

Due to its high oxidizing potential and contribution to the radiative budget, ozone plays an undeniable role in the Earth's atmosphere (IPCC, 2013, 2021; WMO, 2022). In the stratosphere, ozone serves as a protective shield for the biosphere by

1

absorbing the majority of solar ultraviolet radiation (UVR) in the 280–315 nm range (Orphal et al., 2016). This shielding action protects ecosystems and human health from the harmful effects of UV-B radiation, which can lead to adverse health issues such as cataracts, melanoma, and skin aging, while deteriorating materials (Pitts et al., 1977; Matsumura and Ananthaswamy, 2004; Bernhard et al., 2020; Neale et al., 2021). In the past decades, anthropogenic emission of chlorofluorocarbons (CFCs) and halons (including Br) was found to be responsible for the rapid decline in stratospheric ozone (Molina and Rowland, 1974; Solomon, 1988; Rowland, 1996). Within the stratosphere, CFCs are indeed photo-dissociated into chlorine compounds which are known to efficiently deplete ozone (Solomon, 1999). Following the ratification of the Montreal Protocol in 1987, CFC emissions were gradually restricted and forbidden, and previous research and reports show that the ozone layer is expected to return to its 1970s levels from the middle to the end of this century, depending on the latitude (Dhomse et al., 2018; WMO, 2022).

In contrast, tropospheric ozone is a secondary pollutant that directly harms ecosystems, reduces crop productivity, and has negative effects on human health (Mills et al., 2018; Nuvolone et al., 2018). Photochemical formation of tropospheric ozone is driven by the combination of solar radiation and ozone precursors, including volatile organic compounds (VOCs), nitrogen oxides (NO_x) and aerosols (Jacob, 1999; Ivatt et al., 2022). Ozone in the troposphere can therefore be enhanced by anthropogenic activities that release NO_x, aerosols and VOCs, such as agriculture, industry and transport.

Explosive volcanic eruptions can influence stratospheric ozone concentrations, and thus play a role in global chemistry and radiative forcing (Robock, 2000). Previous major eruptions, such as that of Fuego (1974), El Chichón (1982), Mount Pinatubo (1991), Cerro Hudson (1991) and Calbuco (2015) are well-documented examples of events that have altered global atmospheric chemistry (Crafford, 1975; Cadle et al., 1977; Doiron et al., 1991; Gobbi et al., 1992; Schoeberl et al., 1993; McCormick et al., 1995; WMO, 1999; Guo et al., 2004; Kremser et al., 2016; Zhu et al., 2018). Explosive eruptions can release substantial amounts of sulfur dioxide (SO_2), which is subsequently converted into sulfuric acid (H_2SO_4). The resulting sulfuric acid condenses to form sulfate aerosols, secondary volcanic particles which can in turn contribute to stratospheric ozone depletion by increasing the surface area available for heterogeneous chemical reactions. Studies have highlighted the relationship between SO_2 and chlorine in causing ozone decline post-eruption (e.g. Tie and Brasseur (1995); Hofmann and Solomon (1989)). As an example, McCormick et al. (1995) reported that tropical column ozone decreased by 6–8 % in the months following the Mount Pinatubo eruption. They observed that losses were greatest below 28 km, amounting to 20 % in the 24–25 km altitude range. Because of the implied ozone losses and radiative forcing anomalies, the injection of volcanic plumes into the stratosphere can also influence atmospheric temperatures. Ramaswamy et al. (2006) observed increases in global lower stratospheric temperatures following the major eruptions of El Chichón and Mount Pinatubo. Moreover, it was determined that the ozone depletion in the aerosol layer caused by the Mount Pinatubo eruption reduced stratospheric heating by 30 % (Kirchner et al., 1999). Despite this reduction, the radiative anomalies caused by the presence of stratospheric aerosols induced a global stratospheric warming of 3–4 K and tropospheric cooling (Stenchikov et al., 1998; Kirchner et al., 1999).

Moderate and major eruptions may also contribute to the amplitude and dimension of the ozone hole over Antarctica. Following the Mount Pinatubo eruption, Hofmann and Oltmans (1993) observed unusually low total ozone values of 105 DU over the South Pole Station. This deeper ozone hole was attributed to enhanced polar stratospheric clouds (PSCs) volume

driven by extra stratospheric sulfuric acid availability, offering more surface for halogen-ozone reactions. Ivy et al. (2017) reported an increase of the 2015 Antarctic ozone hole by 4.5×10^6 km^2, primarily attributed to volcanic aerosols from the Calbuco eruption. Similarly, Zhu et al. (2018) reported penetration of volcanic sulfate aerosols from the Calbuco eruption into the Antarctic polar vortex, resulting in earlier ozone loss and an increase in the area of the ozone hole. Yook et al. (2022) also hypothesized a link between the eruption of La Soufrière in 2021 and the longevity of the 2021 ozone hole. Hence, numerous research papers focused on ozone chemistry and atmospheric forcings following eruption events.

The Hunga eruption constitutes an unprecedented event of the satellite era (Wright et al., 2022; Carr et al., 2022). The main eruption likely released more energy than the 1991 Mount Pinatubo eruption and caused the largest stratospheric aerosol disturbance since that event (Sellitto et al., 2022; Khaykin et al., 2022; Taha et al., 2022). Its consequences have been under intensive scrutiny, and studies revealed it injected $\sim$0.5 Tg of SO$_2$ and 146 ± 5 Tg of water vapor (H$_2$O) into the stratosphere, corresponding to an increase of $\sim$10 % of the global stratospheric H$_2$O burden (Khaykin et al., 2022; Vömel et al., 2022; Zuo et al., 2022; Millán et al., 2022). The eruption's aerosol column extended through the troposphere and stratosphere, and even reached the lower mesosphere (Carr et al., 2022). Legras et al. (2022) demonstrated that the initial volcanic plume consisted of two distinct sulfate aerosol clouds, which descended from $\sim$30 and $\sim$28 km on 15 January to $\sim$27 and $\sim$25 km by 28 January.

Evan et al. (2023) and Zhu et al. (2023) attribute the initial low ozone levels observed with satellite data to the lofting of ozone-poor tropospheric air masses. However, the subsequent ozone depletion observed in the following days is attributed to chemical processes. Specifically, these studies highlight the role of heterogeneous chlorine activation on humidified volcanic aerosols and gas-phase ozone-depleting reactions. The significant increase in stratospheric humidity facilitated the rapid conversion of SO$_2$ to sulfate aerosols in less than two weeks (Legras et al., 2022; Asher et al., 2023; Zhu et al., 2023). This increase in aerosol surface area, coupled with Hunga-induced stratospheric cooling (Sicard et al., 2024) that enhanced heterogeneous reaction rates, likely accelerated heterogeneous chlorine activation on sulfate aerosols and led to notable ozone depletion despite elevated non-polar temperatures (Evan et al., 2023; Zhu et al., 2023). In this context, Evan et al. (2023) provided evidence of HCl activation on sulfate aerosols within the volcanic plume. The key heterogeneous activation reactions responsible for ozone depletion, as listed by Solomon (1999), are :

$$HCl + ClONO_2 \rightarrow HNO_3 + Cl_2, \tag{R1}$$

$$N_2O_5 + H_2O \rightarrow 2HNO_3, \tag{R2}$$

$$ClONO_2 + H_2O \rightarrow HNO_3 + HOCl, \tag{R3}$$

$$HCl + HOCl \rightarrow H_2O + Cl_2, \tag{R4}$$

$$BrONO_2 + H_2O \rightarrow HNO_3 + HOBr, \tag{R5}$$

$$HCl + BrONO_2 \rightarrow HNO_3 + BrCl, \tag{R6}$$

$$HCl + HOBr \rightarrow H_2O + BrCl. \tag{R7}$$

While heterogeneous reactions played a crucial role in ozone loss, Zhu et al. (2023) also emphasized the importance of gas-phase reactions. In fact, Zhu et al. (2023) and Evan et al. (2023) identified key gas-phase mechanisms contributing to ozone loss: enhanced HO_x cycle activity due to high H_2O concentrations, strengthened interactions between the HO_x and ClO_x cycles (through $HO_2 + ClO \rightarrow HOCl + O_2$), and the slowing down of the NO_x cycle. Thus, Evan et al. (2023) documented a doubling of ozone loss via the reaction $O_3 + Cl \rightarrow O_2 + ClO$ and observed a 5 % depletion of stratospheric ozone over the Indian Ocean within a week post-eruption, with the most significant losses during periods of peak stratospheric humidification.

This study provides the first analysis of ozone observations using Infrared Atmospheric Sounding Interferometer (IASI) (Aires et al., 2002; Blumstein et al., 2004) data following the January 2022 Hunga eruption, focusing on the Indian Ocean and particularly Reunion, where our ground-based measurements are performed. Due to the prevailing westward austral summer stratospheric circulation, the first signs of the Hunga aerosol plume's passage over Reunion were noticed only 4 days after the eruption (Baron et al., 2023; Legras et al., 2022). This study combines local ground-based measurements at Reunion with satellite data over the Indian Ocean, including observations from the Microwave Limb Sounder (MLS) (Waters et al., 2006) and IASI, to examine the impacts of the eruption on ozone during the first 10 days post-eruption. The objectives of the present manuscript can be summarized in three points: firstly, we use IASI observations to demonstrate the appearance of a transient ozone depletion event; secondly, we show the zonal displacement of the SO_2 and H_2O plumes using satellite data; and thirdly, we use MLS ozone profiles traversed by each of the two sulfate aerosol clouds to characterize their respective impacts on ozone.

2 Instrumentation and Method

In this study, we combined ground-based and satellite observational data to investigate the impacts on ozone after the Hunga eruption. The study region encompasses the area bounded by 45° E to 175° E and 30° S to 0°. Satellite observations of ozone profiles and columns were exclusively acquired within this region, complementing the ground-based data while offering global coverage and regular monitoring. This section outlines the different types of data used in our analysis. Unless specified otherwise, all uncertainties, standard errors and standard deviations are reported at the 2σ confidence level.

2.1 Ozone measurements

2.1.1 Lidar observations

A stratospheric DIfferential Absorption Lidar (DIAL) has been operated since January 2013 at the Reunion Atmospheric Physics Observatory (OPAR, 21.08° S; 55.38° E, 2160 m asl) (Baray et al., 2013; Portafaix et al., 2015). This instrument can retrieve ozone concentration profiles at altitudes ranging from 15 to ∼45 km. Lidar observations provide high vertical resolution (Pazmiño, 2006), with typical values ranging from 0.5 km at 15 km to 5 km at 45 km (Godin-Beekmann et al., 2003). The total accuracy is ∼5 % below 20 km, ∼3 % in the 20–30 km altitude range and 15–30 % above 45 km (Godin-Beekmann et al., 2003). However, although the Maïdo DIAL system recorded data during the initial passage of the volcanic plume in

January 2022, the corresponding signal-to-noise ratio (SNR) was extremely low, and the ozone profiles were not reliable. As a result, stratospheric DIAL ozone profiles used in this paper were recorded before the Hunga eruption, from January 2013 to December 2021. The 470 ozone profiles obtained during this period were used to determine the background ozone level for the month of January and were compared with profiles from satellites. As part of the Network for the Detection of Atmospheric Composition Change (NDACC), this DIAL data can be accessed at the following link: https://ndacc.larc.nasa.gov/ (last accessed on 23 January 2024).

2.1.2 SAOZ measurements

The Système d'Analyse par Observation Zénithale (SAOZ), an instrument also integrated into the NDACC, is a ground-based spectrometer which measures the sunlight scattered from the zenith sky within the 300 to 650 nm range (Pommereau and Goutail, 1988). Differential Optical Absorption Spectrometry (DOAS) is utilized to analyze observations, enabling the retrieval of daily ozone and nitrogen columns at sunrise and sunset with a total accuracy of 6 % and 14 %, respectively (Boynard et al., 2018). Operating at an altitude of 80 m asl in Saint-Denis (20.90° S; 55.48° E), Reunion, since 1993, a SAOZ instrument has provided Total Column Ozone (TCO) observations at this subtropical site for over three decades. Unfortunately, SAOZ data during the passage of the aerosol plume over Reunion are unreliable because of an unrealistic representation of the Air Mass Factor (AMF), leading to biased TCO retrievals. Consequently, SAOZ data for January 2022 were excluded. However, data outside this time period and climatological values of TCO for the month of January (262.8 ± 11.9 DU) were kept to illustrate the background January ozone TCO. The SAOZ data used in this work can be downloaded from this website: http://saoz.obs.uvsq.fr/ (last accessed on 23 January 2024).

2.1.3 MLS profiles

The MLS instrument is located on the Aura satellite, launched in July 2004. The Aura satellite follows a helio-synchronous orbit and passes the equator at 01:45 pm local solar time on its ascending node. In order to observe atmospheric parameters like temperature and atmospheric component concentrations, MLS measures thermal radiation emitted from the Earth's atmospheric limb ahead of its orbital path at spectral wavelengths ranging from 0.12 to 2.5 mm (Waters et al., 2006). According to Millán et al. (2022), observations inside the Hunga plume should be studied using MLS data at level 2 and version 4 (v4), instead of the latest version (v5). Indeed, both MLS versions use different instrument pointing methods. While v4 relies only on pointing from O_2 signals, v5 also uses the H_2O line. This inclusion may degrade results in regions of enhanced humidity, which are common in our study. Additionally, their study indicates that the quality of ozone and temperature measurements are not affected by the aerosol plume (Millán et al., 2022).

Following these recommendations, the MLS profiles for January 2022 are sourced exclusively from level 2 v4 measurements (Livesey et al., 2020) and categorized as either Hunga-influenced or non-influenced. The criterion for this distinction is detailed in the next paragraph. To evaluate the similarity between v4 and v5 MLS ozone profiles during unperturbed conditions, we calculated the differences for the colocated v4 and v5 non-influenced ozone profiles. The maximum standard deviation did not exceed 0.1 ppmv in any of the 10 to 100 hPa pressure levels, corresponding to a 0.02% variation relative to mean ozone volume

mixing ratio in this region, demonstrating the similarity of these two versions during background conditions. Additionally, to assess the similarity between v5 MLS ozone profiles and the Reunion DIAL profiles, we performed an inter-comparison procedure detailed in Section 2.4. To compare v4 Hunga-influenced ozone profiles to background non-influenced profiles, we employed MLS level 2 v5 data (Livesey et al., 2022). All v5 ozone and water vapor profiles within a 5-degree radius of each of the January 2022 Hunga-influenced profiles were collected, regardless of the satellite's ascending or descending node. This procedure was undertaken for each day for the months of January from 2013 to 2021 to derive the monthly averaged background profiles. This specific time period was chosen to align with the lidar time series.

The selection of v4 MLS Hunga-influenced profiles is based on an adaptation of the criterion from Evan et al. (2023). First, similar to their procedure, locations with v4 water vapor profiles exhibiting mixing ratio values exceeding 100 ppmv within the 10 to 100 hPa range were identified. Next, following the findings of Legras et al. (2022), the criterion was refined to classify as Hunga-influenced only those ozone profiles affected by one of the two sulfate aerosol clouds located at approximately 25 km and 28 km (corresponding to the 26.10 and 14.68 hPa MLS pressure levels, respectively). Locations showing high water vapor and a negative ozone anomaly at one of these pressure levels were classified as Hunga-influenced. Applying this refined criterion yielded 72 Hunga-influenced (and 2215 non-influenced) ozone and water vapor profiles between 15 and 23 January over the Indian Ocean. Of the Hunga-influenced profiles, 52 were impacted by the highest aerosol cloud (at ∼28 km), and 20 by the lowest one (at ∼25 km). Both profile groups were analyzed separately to characterize the individual impacts of each sulfate aerosol cloud on ozone.

In most of the stratosphere, specifically between 1 and 68 hPa, MLS ozone volume mixing ratio profiles have accuracy and precision that are both better than 10 % (Livesey et al., 2022). In accordance with the recommendations made in the MLS data quality and description documents, all quality flags (quality, convergence, status and precision) were used on the raw profiles (with the exception of the v4 H_2O profiles), and data lying outside the recommended range (261 to 0.001 hPa, or approximately 11 to 90 km) were not used (Livesey et al., 2022, 2020). Only the v5 and v4 O_3 profiles were screened following the procedures stated within these documents. MLS observations can be accessed through NASA's data portal (https://disc.gsfc.nasa.gov/, last accessed on 23 January 2024).

2.1.4 IASI maps

IASI is a Fourier Transform spectrometer installed on the three Metop satellites (Clerbaux et al., 2009; Coheur et al., 2009). This instrument retrieves ozone profiles by analyzing day and night nadir radiances within the thermal infrared spectrum from 6.62 to 15.5 μm. In the present study, we used data obtained from the Fast-Optimal Retrievals on Layers for IASI (FORLI-O3) ozone products (Hurtmans et al., 2012), which have been extensively validated (Boynard et al., 2018). Specifically, to study the impact of the Hunga eruption on ozone levels in January 2022, we employed a combination of daily TCO observations and daily ozone partial columns from IASI instruments onboard Metop-B and Metop-C, operational since 2013 and 2019, respectively. To obtain average TCO maps during unperturbed conditions, we used monthly TCO data exclusively from IASI on Metop-B. Given that IASI on Metop-B has been providing measurements since March 2013, we used the average of TCO maps spanning from January 2014 to 2021 as being representative of ozone background. Unlike daily TCO, monthly TCO

data points from IASI are re-sampled to be distributed on a regular grid. Therefore, to compute anomalies, we performed a re-sampling of daily data to align with the monthly grid. At each grid location, the nearest daily IASI TCO observation within a 0.5° radius was interpolated. If the closest observations lie beyond this radius limit, then no value was kept for this grid point. Consequently, TCO anomalies from IASI represent the difference between the background ozone levels (from monthly data) and a re-sampled combination of Metop-B and Metop-C daily data during the Hunga event. Similarly, we derived Stratospheric Column Ozone (SCO) maps by summing the ozone partial columns above the altitude of the tropopause, as estimated by the instrument. The unperturbed average SCO map was calculated using all daily IASI profiles from Metop-B for the months of January from 2014 to 2021 and re-sampled onto the monthly grid using the same methodology described earlier. To observe the spatial correlation between the ozone anomaly, the water vapor anomaly and the SO_2 plume, we also employed daily SO_2 observations from Metop-B and Metop-C (Clarisse et al., 2012, 2014). The IASI products employed in this work can be accessed on the AERIS platform: https://iasi.aeris-data.fr (last accessed on 23 January 2024).

In contrast to UV-visible instruments, which reported significant ozone perturbations following the eruption (attributed to interference from SO_2 and H_2SO_4), no similar disturbances were observed in the IASI ozone retrievals. Because the spectral ranges of ozone and SO_2 do not overlap in the IASI ozone retrieval, results should not show any bias. While sulfate aerosols may share some spectral range with ozone, the retrieval algorithm can distinguish between the two, as sulfate aerosols exhibit strong absorption features and ozone variations are directly measured through its absorption lines. Thus, the IASI algorithm should account for ozone vertical variability effectively following the Hunga eruption.

2.2 Aerosol measurements

In addition to the DIAL system, the OPAR is equipped with several other active remote sensing systems, including a Rayleigh-Mie lidar for aerosol profile measurements (Baron et al., 2023). In this study we used aerosol extinction profiles together with the corresponding stratospheric Aerosol Optical Depth (sAOD) at 532 nm as derived from the Rayleigh-Mie lidar measurements at the Reunion observatory. The data used in this study are publicly accessible via this webpage: https://geosur.osureunion.fr/geonetwork/srv/eng/catalog.search#/metadata/f2c35798-47b7-433c-8927-46cf7babca83. The L2 ready-to-use data set in netCDF format can be accessed from Baron (2023) (last accessed on 23 January 2024).

Aerosol optical properties can also be retrieved using sun-photometers. These remote sensing sun-tracking radiometers perform regular and frequent measurements of the direct solar spectral irradiance, typically at wavelengths between 340 and 1640 nm. By comparing the ground solar irradiance to the estimated top of the atmosphere irradiance, they can determine the total AOD, a quantity that describes the opacity of the atmosphere to radiation. Therefore, a sun-photometer gives a measure of aerosol abundance in the atmospheric column above the study site. In the present study, we used AOD data from a Cimel sun-photometer located at the Saint-Denis campus, which has been operating since December 2003 in the framework of the AErosol RObotic NETwork (AERONET) program. We used level 2.0 v3 AERONET data for the period from December 2003 to January 2022. AERONET data of level 2.0 is quality-controlled with near-real time automatic cloud-screening in addition to having pre- and post-field calibrations. According to Giles et al. (2019), the 1σ uncertainty for the near-real time AERONET AOD

measurement is up to 0.02. AERONET data are accessible from https://aeronet.gsfc.nasa.gov/ (last accessed on 23 January 2024).

The Ozone Mapping and Profiler Suite Limb Profiler (OMPS-LP) monitors the Earth limb ahead of its orbit path to provide high vertical resolution ozone and aerosol profiles. The instrument measures limb scattering radiances in the 290–1000 nm wavelength range over the sunlit portion of the atmosphere using three vertical slits. This instrument has been making observations onboard the Suomi National Polar-orbiting Partnership (Suomi NPP) spacecraft since January 2012, following a helio-synchronous orbit with an equatorial passing time of 01:30 pm solar time on its ascending node. With the goal to study the spatial extension of the plume, we used OMPS-LP aerosol extinction profiles at 745 nm. According to Taha et al. (2021), extinction coefficients at 745 nm have relative accuracy and precision of 10 % and 15 %, respectively. OMPS data were downloaded from the following link: https://ozoneaq.gsfc.nasa.gov/ (last accessed on 05 March 2024).

2.3 Trajectory model

To investigate the origin of the air masses in our study region, we used the HYbrid Single Particle Lagrangian Integrated Trajectory (HYSPLIT) model in its passive and backward mode (Draxler and Hess, 1997, 1998). Developed by the National Oceanic and Atmospheric Administration (NOAA), this model uses meteorological fields to compute trajectories of air masses. We used a single HYSPLIT simulation of the trajectories of air masses in the stratosphere over the Indian Ocean. Thus, using meteorological fields from the Global Data Assimilation System (GDAS) (National Oceanic and Atmospheric Administration (NOAA), 2023), we ran a 240-hour back trajectory simulation of 12 distinct air parcels with terminal altitudes distributed equally between 23.5 and 29.0 km. These trajectories were chosen to have their endpoint at the location of Saint-Denis, Reunion. HYSPLIT trajectories can be obtained by running simulations through the following link: https://www.ready.noaa.gov/HYSPLIT_traj.php (last accessed on 23 January 2024).

2.4 Inter-comparison

Prior to drawing any conclusions based on the MLS ozone profiles, it is essential to verify their agreement with precise local lidar observations during unperturbed conditions. For this inter-comparison process, we determined daily MLS ozone profiles by averaging all recovered profiles within a 5-degree region around the lidar site, setting the inter-comparison radius to a maximum of 5°. We used MLS v5 ozone profiles from both ascending and descending Aura orbits, with acquisition times near Reunion around 10:15 and 21:45 UTC, respectively. Profiles from both orbit types were averaged together, with no distinction made between ascending and descending data. On the other hand, the 470 ground-based DIAL lidar profiles are only nocturnal (recorded at Reunion, i.e. approximately between 16:00 and 01:00 UTC, averaging around 18:30 UTC). Thus, the maximum temporal difference between MLS and lidar profiles is approximately 8 hours. Despite the non-overlapping acquisition times, we compared DIAL night profiles to daily MLS profiles. Although we obtained 470 DIAL profiles, the 5° inter-comparison radius limits the number of available MLS profiles, allowing inter-comparison on a total of 340 days. Since lidar profiles use altitude as the vertical coordinate and MLS retrievals are output on a pressure grid, we first converted the MLS pressure grid to an altitude grid using MLS geopotential height profiles. Following Sections 1.8 and 1.9 of Livesey et al. (2022),

the comparison with lidar profiles was then conducted by applying MLS averaging kernels and a priori ozone profiles, after reducing the resolution of the lidar profiles using least-squares smoothing. As a result, the profile comparison is based on the following formula:

$$\text{Relative}_{\text{bias}}(z) = 100 \times \frac{\text{O}_{3\text{ MLS}}(z) - \text{O}_{3\text{ DIAL}}(z)}{\text{O}_{3\text{ DIAL}}(z)}, \tag{1}$$

where $\text{O}_{3\text{ MLS}}(z)$ represents the MLS ozone value from averaging kernel at an altitude z and $\text{O}_{3\text{ DIAL}}(z)$ represents the smoothed stratospheric DIAL ozone value at the same altitude. Other statistical quantities were also determined, namely the number of profiles (N), the coefficient of correlation (r), the linear regression (in the form $y = ax$) and the Root-Mean-Square Dispersion (RMSD). These statistical quantities were used to assess the differences and similarities between different ozone data at different layers.

Additionally, to compare IASI data with SAOZ measurements recovered at Reunion under unperturbed conditions, we derived a daily TCO time series from Metop-B at Reunion, spanning March 2013 to December 2021. The inter-comparison utilized all data points from both datasets within this time period, irrespective of date and time of day, including all sunrise and sunset measurements.

3   Results and discussion

3.1   Aerosol plume

The Hunga main eruption occurred on 15 January 2022 and ejected a large quantity of H_2O and a moderate amount of SO_2 into the stratosphere (Khaykin et al., 2022; Sellitto et al., 2022; Zuo et al., 2022; Millán et al., 2022). Following the austral summer's general stratospheric circulation, the volcanic plume then traveled westward and reached the Indian Ocean and the African continent within days (Baron et al., 2023). The aerosol plume's transport across the Indian Ocean was captured by OMPS aerosol extinction profiles. Panel (a) of Fig. 1 shows the background aerosol distribution at 745 nm over the Indian Ocean, captured prior to the arrival of the volcanic plume. Panels (b) to (e) present OMPS extinction coefficient profiles across different locations in the Indian Ocean as a function of latitude and altitude during the passage of the volcanic plume. At the bottom left of each panel are given the date and time of retrieval, the black dots correspond to the instrument's estimation of the tropopause height and the vertical dashed lines mark the positions of the 5° S and 25° S latitude lines. Panel (f) traces the satellite tracks corresponding to data in panels (a) to (e). Thus, this figure describes the latitudinal and vertical extent of the volcanic plume as observed by the satellite instrument during its passage over the Indian Ocean on 22 January, the date when impacts on ozone at Reunion were highest (Evan et al., 2023). During unperturbed conditions (see Fig. 1a), the aerosol distribution shows that the largest values of the extinction coefficient are kept below the tropopause. Aerosol presence in the stratosphere is negligible compared to that in the troposphere. However, the presence of the volcanic plume becomes clearly visible on the other panels, where large extinction coefficient values ($> 10^{-3}$) lie above the tropopause level and become comparable to those typically observed in the upper troposphere. On 22 January (Fig. 1b to 1e), the volcanic plume is clearly

visible in the stratosphere over the Indian Ocean between 5° S and 25° S, reaching altitudes greater than 35 km. Note that this result only characterizes the vertical and latitudinal extent of the volcanic plume, but it does not describe the longitudinal dimension of the plume. Equivalent observations can also be obtained for 21 January (not shown). Similar results were found by Taha et al. (2022) as they outlined the presence of a volcanic plume located at an altitude exceeding 36 km. Additionally, they reported that the high sensitivity of OMPS LP enabled the monitoring of the volcanic plume at altitudes above 36 km for a duration of up to 90 days.

Figure 2 shows the Hunga aerosol plume as seen by two quasi-colocated instruments operating at the Maïdo observatory (lidar) and the Saint-Denis campus (sun-photometer). It is important to emphasize that the two instruments are 20 km apart with an approximately 2000 m difference in elevation. Even though the total AOD measured by the sun-photometer cannot be directly compared to the sAOD recorded by the lidar instrument, both sets of observations hold significant information about the passage of the volcanic plume. Figure 2a depicts the evolution of the lidar aerosol extinction profiles at 532 nm between 21 and 23 January, and Fig. 2b shows the evolution of the lidar sAOD at 532 nm (in black) and sun-photometer level 2.0 total AOD at 532 nm (in red) for the second half of January 2022. The lidar sAOD uncertainty is represented by the shading, while the sun-photometer AOD uncertainty, assumed to be of 0.02 (1σ) for all measurements (Giles et al., 2019), is illustrated in the upper part of the panel at the 2σ level. The sun-photometer AOD at 532 nm was obtained from the conversion of the AOD at 675 nm using the Angström exponent measurements between 440 and 675 nm. The blue line represents the multi-year average of sun-photometer level 2.0 AOD data for January, calculated from 2003 to 2021, with the shaded blue region indicating the corresponding standard deviation. Note that different horizontal axes are used for panels (a) and (b), and the common observation periods are enclosed by vertical dashed lines in the two panels.

Results show that the maximum total and stratospheric optical depths recorded by both instruments in January 2022 are very high in comparison to the multi-year mean AOD of 0.05 ± 0.04. This is expected, as Reunion is a pristine region where January usually experiences low AOD levels (Duflot et al., 2022). After 20 January, total AOD values start to dramatically increase until 23 January, when they culminated at 0.57 ± 0.04 before gradually decreasing to return to background levels. Similar to the sun-photometer measurements, the Maïdo lidar reveals a large amount of aerosols after 21 January, with sAOD values rising up to 0.84 ± 0.27. A significant aerosol layer was seen by the lidar on two consecutive nights at altitudes of 29.7 km and 26.8 km, with maximum extinction coefficients of 0.53 ± 0.17 and 0.68 ± 0.11, respectively. Note that sun-photometer measurements are obtained during the day, while lidar observations are only performed during nighttime. As such, observations from these two instruments cannot overlap as they do not operate simultaneously. A detailed study of the lidar observation of the Hunga plume can be found in Baron et al. (2023). Our results support their research, suggesting that the bulk of the Hunga aerosol plume passed over Reunion from 21 to 23 January.

3.2 Maïdo DIAL and MLS average ozone profiles

Figure 3 shows the average January Maïdo DIAL ozone profile, with the blue shaded area indicating the standard deviation. The orange and green lines represent the average January MLS ozone profiles representative of Reunion and the full study region, respectively, with standard deviations shown as horizontal bars. The averages of all profiles remain within each other's standard

deviation. Above 37 km, the average lidar profile slightly diverges from the average MLS profiles, likely due to decreased lidar

315 SNR and fewer available profiles, also increasing the standard variation. Still, average profiles are similar in the 15–37 km range. Because of the similarity between the lidar and MLS average profiles over Reunion up to ∼30 km (the altitude of the highest aerosol cloud), MLS appears to be a suitable substitute for lidar data in studying ozone levels. Additionally, the strong agreement between MLS averages for Reunion and the entire study region supports the use of MLS data across the region, suggesting that ozone levels at Reunion are representative of background levels over the Indian Ocean.

320 With a predominant annual cycle (not shown), the ozone maximum at Reunion is at its highest altitude during austral summer, and at its lowest altitude during austral winter. This behavior, observed in subtropical (e.g., Reunion, which is located at the edge of the tropical barrier in the stratosphere) and tropical locations, is primarily attributed to dynamical processes. Notably, tropical upwelling, as part of the Brewer-Dobson Circulation (BDC), transports ozone from the equator (where it is primarily produced) to higher latitudes (Butchart, 2014; Plumb and Eluszkiewicz, 1999; Weber et al., 2011). During austral

325 summer (winter), Reunion is closest to the ascending (descending) branch of the BDC, which explains why the ozone layer is highest (lowest) in altitude at that time.

3.3 Inter-comparison results

Before analyzing ozone measurements and stratospheric transport, we conducted a statistical analysis to evaluate differences between lidar and MLS observations, as well as between IASI and SAOZ data, under unperturbed conditions. For this pur-

330 pose, we compared two datasets: 1) MLS v5 ozone volume mixing ratio profiles over Reunion with Reunion's stratospheric DIAL ozone profiles, covering January 2013 to December 2021; and 2) SAOZ TCO with IASI TCO, covering March 2013 to December 2021.

Results are presented in Fig. 4, with panels (a) and (b) displaying the MLS-DIAL and SAOZ-IASI comparisons, respectively. The continuous line and the shaded area in Fig. 4a represent the mean relative bias and the standard error, respectively. This

335 standard error represents the standard deviation divided by the square root of the number of individual comparisons (which varies as a function of altitude). The aforementioned statistical quantities are also shown in the figure. These mean relative bias profiles were obtained by averaging the relative bias values as derived from Eq. (1) across all available ozone profiles. Statistical results (correlation coefficient, linear regression and relative RMSD) presented in the following paragraphs were obtained from the comparison of all data points, irrespective of the altitude level, date and time of day.

340 Concerning ozone profiles, the best agreement is found in the 20–40 km altitude range, with higher and increasing deviations below 20 km and above 40 km. In the altitude range from 20 to 40 km, MLS has a relative bias and error (i.e. relative bias and error averaged over the 20–40 km altitude range, with respect to DIAL measurements) of 0.11 ± 0.20 %. In this altitude range, the standard error is low because of the large number of available comparison profiles (up to a maximum of 340). From 40 to 45 km, the bias decreases to 0.24 ± 2.12 %, whereas below 20 km, it shows an average of 2.44 ± 2.04 %. The increased

345 difference and error at altitudes greater than 40 km is partly due to the lidar SNR decrease and the reduced number of lidar profiles reaching altitudes greater than 45 km. The decrease in SNR requires additional signal filtering, which introduces a high bias of ozone lidar profile with respect to other measurements (Godin et al., 1999). Consequently, the lidar mean measurement

error increases from $\sim 10\%$ at 40 km to $\sim 50\%$ at 47.5 km. Additionally, out of the 470 lidar profiles, 410 reached 40 km, 132 reached 45 km and only 6 reached 47.5 km. Note also that the increased difference and error at altitudes lower than 20 km may
350   be due to the reduced satellite accuracy and precision (see Table 3.18.1 of Livesey et al. (2022)) and the smaller number of lidar profiles for these altitudes. Indeed, out of the 470 profiles, only 453 extend below 20 km, 409 below 17.5 km and 131 below 15 km. Over the whole altitude range, the correlation coefficient (r = 0.99) indicates an excellent correlation between the lidar and MLS, and the linear regression ($y = 0.99\,x$) shows that MLS profiles tend to slightly under-estimate ozone concentrations relative to DIAL, irrespective of the altitude. Finally, a low relative dispersion (RMSD = 1.27 %) further demonstrates the
355   agreement between MLS and the DIAL profiles.

Concerning TCO data, the large number of comparison points (N = 5619) enables precise statistics, indicating very low relative dispersion (RMSD = 3.26 %) and an elevated correlation (r = 0.87) between IASI and SAOZ datasets. The linear regression ($y = 1.02\,x$) shows that IASI TCO tends to slightly over-estimate SAOZ TCO.

Therefore, the MLS ozone profiles are in good agreement with lidar observations in the 20–40 km altitude range, which
360   includes the altitudes of the Hunga volcanic plume (25–30 km) being our main focus in this study. The IASI and SAOZ TCO also exhibit low dispersion and a high degree of correlation throughout the comparison period.

3.4 Effects of the volcanic plume on ozone

Based on the excellent correlation and agreement between satellite (MLS and IASI) and ground-based (stratospheric lidar and SAOZ) instruments over Reunion, it appears relevant to use satellite ozone products to investigate the changes in the
365   distribution of ozone over the study region.

Figure 5 depicts daily maps of SCO (panels (a1) to (a9)), significant SCO anomalies at the 2σ level (panels (b1) to (b9)) and total SO_2 (panels (c1) to (c9)) over the Indian Ocean from 15 to 23 January. All maps are overlaid with red contours of the SO_2 plume, indicating regions where the SO_2 total column is greater than 30 DU. SO_2 maps are complemented by the MLS satellite track (blue circles), with the MLS profiles meeting the selection criterion marked by dark blue circles. The successive
370   locations of the SO_2 plume and the Hunga-influenced MLS profiles, which capture the H_2O and ozone anomalies, reveal an east-to-west displacement of both plumes. The parallel displacement of the SO_2 and H_2O plumes supports previous studies, and the rapid disappearance of the high SO_2 anomaly indicates its rapid conversion into sulfates under the influence of H_2O (Legras et al., 2022; Zhu et al., 2023; Asher et al., 2023).

This zonal movement is also reflected in SCO and SCO anomalies from IASI, illustrating a correlation between ozone,
375   H_2O and SO_2 anomalies. The first significant negative ozone anomaly linked to the Hunga appears on 15 January at 169.5° E, with a value of -23.5 $\pm$ 4.8 DU, with the error indicating the 2σ uncertainty in both the anomaly and SCO values from IASI observations. This first ozone anomaly is attributed to the lofting of ozone-poor tropospheric air masses (Zhu et al., 2023; Evan et al., 2023). This anomaly then appears to grow larger in size and amplitude as the SO_2 plume spreads, despite cloud cover on 18 January hindering IASI observations, before reaching Reunion on 21 January. The rapid conversion of SO_2 molecules to
380   sulfate particles in the first days following the eruption increased the aerosol surface area, resulting in ozone depletion through

heterogeneous chemistry (Zhu et al., 2023; Evan et al., 2023). This rapid conversion is evidenced by the gradual disappearance of the SO_2 contour in red, which correlates with the increase in ozone anomaly.

On 20 and 21 January, when stratospheric ozone depletion is best seen in panels a6–a7 and b6–b7, IASI recorded minimum SCO values and maximum associated anomalies. On 21 January, record anomalies of -49.9 $\pm$ 4.7 DU were recorded 76.5° E. Compared to the IASI average SCO values for January at the same location (227.0 $\pm$ 3.5 DU), this IASI SCO anomaly is more than 14 times below the average variability. The IASI anomaly map for 20 and 21 January suggests the appearance of a large transient ozone depletion event extending over approximately 30 degrees of longitude and 20 degrees of latitude. The presence of clouds on 22 January hindered the retrieval of IASI data between Reunion and Madagascar, but large anomalies were still visible in the region on 23 January. The ozone anomaly then exited the Indian Ocean (not shown). Therefore, the anomaly maps and MLS satellite track emphasize that the study region was subject to SCO and H_2O anomalies over the latitudinal band from 30° S to 10° S, with a zonal westward shift of the ozone minimum. Similar to the findings of Evan et al. (2023), our results indicate the colocation of the H_2O and ozone anomalies as the Hunga plume passed over the Indian Ocean. For zoomed-in results from 21 January, when the anomaly is most pronounced and passes over Reunion, the reader is invited to refer to Fig. A1 in the Appendix.

MLS profiles selected by the criterion were studied further. For each group of Hunga-influenced H_2O and ozone profiles, we computed the difference from their corresponding background average profiles. Subsequently, these individual differences were averaged, and results are presented in panels (a) and (b) of Fig. 6, where the horizontal bars represent the $\pm$ 1σ standard deviation around the mean value. Panels (c) and (d) present the same data on an altitude grid, with ozone anomaly profiles converted to partial columns using geopotential and temperature information. Panel (e) displays the mean January lidar profile along with its 2σ standard deviation, as well as the average MLS ozone profiles influenced by one of the aerosol clouds, accompanied by their respective 1σ standard deviation. These results show that, for each aerosol cloud, the criterion leads to profiles with significant ozone loss at 1σ and water vapor excess at the same pressure ranges.

The ozone mean anomaly associated with the highest aerosol cloud is (1σ) significant at three distinct pressure levels within the 17.78—12.12 hPa range (27–29 km range), with an average anomaly of -0.7 $\pm$ 0.5 ppmv (-1.1 $\pm$ 0.7 DU/km). For the lowest aerosol cloud, significant ozone anomalies occur at the 26.10 and 31.62 hPa levels (23.5 and 24.5 km altitude), with a mean anomaly of -0.6 $\pm$ 0.5 ppmv (-1.7 $\pm$ 1.4 DU/km). Average MLS profiles in Fig. 6e themselves illustrate ozone reduction in altitudes corresponding to the sulfate aerosol clouds and high H_2O anomalies. Compared to the average lidar profile, the ozone depletion observed by MLS from the highest aerosol cloud corresponds to a volume mixing ratio anomaly of -6.3 $\pm$ 5.2 %, while the lowest cloud shows an anomaly of -7.3 $\pm$ 3.0 %. These results are coherent with Evan et al. (2023) who documented a 5 % depletion of stratospheric ozone over the Indian Ocean.

While Figures 5 and A1 revealed local SCO and TCO minima, Fig. 6 shows clear reduction in stratospheric ozone (in the range 30–12 hPa, corresponding to 23.5–30.0 km) linked to sulfate aerosols and excess water vapor. This observation confirms previous research and indicates that the ozone anomaly is linked to a reduction of the ozone layer.

3.5 Transport of air masses in the stratosphere

The Lagrangian HYSPLIT model was used to investigate the origin of the air masses responsible for the ozone anomaly over the Indian Ocean following the Hunga eruption. Back trajectories were run from the location of Reunion on 21 January at 00:00 for 12 distinct altitudes ranging between 23.5 and 29.0 km. Figure 7 shows the result of the HYSPLIT simulation with a color gradient to distinguish different air parcels. The orange trajectory represents air masses at 29.0 km altitude, and the black trajectory represents air masses at 23.5 km. Figure 7 shows that all back trajectories are zonal, moving westward and passing over the location of the Hunga eruption. The results of the HYSPLIT back trajectories simulation are consistent with the lidar measurements made in Reunion (see Fig. 2), as well as with the ozone anomalies over the region of study as depicted in Fig. 5. Additionally, the latter shows a westward transition of ozone anomalies in the stratosphere over the Indian Ocean.

4 Conclusions

The main eruption of the Hunga volcano released significant amounts water vapor and a moderate quantity of sulfur dioxide into the atmosphere (Sellitto et al., 2022; Zuo et al., 2022; Millán et al., 2022), resulting in substantial anomalies within the stratosphere. This study showed the evolution of the colocated ozone, water vapor and SO_2 anomalies in the early Hunga volcanic plume over the Indian Ocean using IASI and MLS observations.

OMPS aerosol extinction profiles revealed that the volcanic plume extended through the stratosphere, from 5° S to 25° S, and reached altitudes greater than 35 km over the Indian Ocean. These results are supported by the Maïdo aerosol lidar, which observed the plume during two consecutive nights a few days after the eruption, indicating that the core of the plume was passing over Reunion at an altitude ranging from 26.8 to 29.7 km. Lidar sAOD and sun-photometer total AOD recorded unprecedented values of 0.84 ± 0.27 and 0.57 ± 0.04, respectively, during the passage of the plume.

The ozone anomaly associated with the volcanic plume was investigated using MLS and IASI ozone data. Based on these results, we state that the advection of the volcanic aerosol and water vapor plumes had an impact on stratospheric ozone levels over the Indian Ocean. As indicated by IASI, a transient ozone depletion event was observed over the region on 21 January, with record TCO and SCO anomalies of -40.1 ± 4.8 DU and -49.9 ± 4.7 DU, respectively. Hunga-influenced MLS profiles indicated significant ozone reduction occurred within the 30–12 hPa pressure range. These ozone reductions occur at two distinct pressure ranges, and are associated to both sulfate aerosol clouds. The highest aerosol cloud decrease ozone levels with an average of -0.7 ± 0.5 ppmv (-1.1 ± 0.7 DU/km) in the 17.78—12.12 hPa range. The lowest aerosol cloud significantly impacted ozone at the 26.10 and 31.62 hPa levels, causing a mean anomaly of -0.6 ± 0.5 ppmv (-1.7 ± 1.4 DU/km).

Appendix A: Appendix A

This section presents satellite observations for 21 January, when the transient ozone depletion event is best seen and passes over Reunion. Figure A1 depicts IASI TCO, SCO and related significant anomalies at the 2σ level, as well as the location of the SO_2 plume from IASI and the Hunga-influenced MLS profiles. Results show significant ozone negative anomalies, both in

TCO and SCO. On this date, record anomalies were observed, with values of -40.1 ± 4.8 DU for TCO and -49.9 ± 4.7 DU for SCO, both located at 76.5° E. Compared to the SAOZ climatological TCO values for January (262.8 ± 11.9 DU), this IASI TCO anomaly is more than 3 times below the climatological variability. Likewise, the January mean TCO value from IASI at the same location (257.0 ± 8.0 DU) shows that this anomaly is about 5 times below the variability derived from IASI data.

References

Aires, F., Rossow, W. B., Scott, N. A., and Chédin, A.: Remote sensing from the infrared atmospheric sounding interferometer instrument 2. Simultaneous retrieval of temperature, water vapor, and ozone atmospheric profiles, Journal of Geophysical Research: Atmospheres, 107, ACH 7–1–ACH 7–12, https://doi.org/https://doi.org/10.1029/2001JD001591, 2002.

Asher, E., Todt, M., Rosenlof, K., Thornberry, T., Gao, R.-S., Taha, G., Walter, P., Alvarez, S., Flynn, J., Davis, S. M., Evan, S., Brioude, J., Metzger, J.-M., Hurst, D. F., Hall, E., and Xiong, K.: Unexpectedly rapid aerosol formation in the Hunga Tonga plume, Proceedings of the National Academy of Sciences, 120, e2219547 120, https://doi.org/10.1073/pnas.2219547120, 2023.

Baray, J. L., Courcoux, Y., Keckhut, P., Portafaix, T., Tulet, P., Cammas, J. P., Hauchecorne, A., Godin Beekmann, S., De Mazière, M., Hermans, C., Desmet, F., Sellegri, K., Colomb, A., Ramonet, M., Sciare, J., Vuillemin, C., Hoareau, C., Dionisi, D., Duflot, V., Vérèmes, H., Porteneuve, J., Gabarrot, F., Gaudo, T., Metzger, J. M., Payen, G., Leclair de Bellevue, J., Barthe, C., Posny, F., Ricaud, P., Abchiche, A., and Delmas, R.: Maïdo observatory: a new high-altitude station facility at Reunion Island (21° S, 55° E) for long-term atmospheric remote sensing and in situ measurements, Atmospheric Measurement Techniques, 6, 2865–2877, https://doi.org/10.5194/amt-6-2865-2013, 2013.

Baron, A., Chazette, P., Khaykin, S., Payen, G., Marquestaut, N., Bègue, N., and Duflot, V.: Early Evolution of the Stratospheric Aerosol Plume Following the 2022 Hunga Tonga-Hunga Ha'apai Eruption: Lidar Observations From Reunion (21°S, 55°E), Geophysical Research Letters, 50, e2022GL101 751, https://doi.org/https://doi.org/10.1029/2022GL101751, e2022GL101751 2022GL101751, 2023.

Baron, A. A.: Early Evolution of the Stratospheric Aerosol Plume Following the 2022 Hunga Tonga-Hunga Ha'apai Eruption: Lidar Observations from Reunion Island (21°S, 55°E), https://doi.org/10.5281/zenodo.7790284, 2023.

Bernhard, G. H., Neale, R. E., Barnes, P. W., Neale, P. J., Zepp, R. G., Wilson, S. R., Andrady, A. L., Bais, A. F., McKenzie, R. L., Aucamp, P. J., Young, P. J., Liley, J. B., Lucas, R. M., Yazar, S., Rhodes, L. E., Byrne, S. N., Hollestein, L. M., Olsen, C. M., Young, A. R., Robson, T. M., Bornman, J. F., Jansen, M. A. K., Robinson, S. A., Ballaré, C. L., Williamson, C. E., Rose, K. C., Banaszak, A. T., Häder, D.-P., Hylander, S., Wängberg, S.-Å., Austin, A. T., Hou, W.-C., Paul, N. D., Madronich, S., Sulzberger, B., Solomon, K. R., Li, H., Schikowski, T., Longstreth, J., Pandey, K. K., Heikkilä, A. M., and White, C. C.: Environmental effects of stratospheric ozone depletion, UV radiation and interactions with climate change: UNEP Environmental Effects Assessment Panel, update 2019, Photochem. Photobiol. Sci., 19, 542–584, https://doi.org/10.1039/D0PP90011G, 2020.

Blumstein, D., Chalon, G., Carlier, T., Buil, C., Hebert, P., Maciaszek, T., Ponce, G., Phulpin, T., Tournier, B., Simeoni, D., Astruc, P., Clauss, A., Kayal, G., and Jegou, R.: IASI instrument: technical overview and measured performances, in: Infrared Spaceborne Remote Sensing XII, edited by Strojnik, M., vol. 5543, pp. 196 – 207, International Society for Optics and Photonics, SPIE, https://doi.org/10.1117/12.560907, 2004.

Boynard, A., Hurtmans, D., Garane, K., Goutail, F., Hadji-Lazaro, J., Elissavet Koukouli, M., Wespes, C., Vigouroux, C., Keppens, A., Pommereau, J.-P., Pazmino, A., Balis, D., Loyola, D., Valks, P., Sussmann, R., Smale, D., Coheur, P.-F., and Clerbaux, C.: Validation of the IASI FORLI/EUMETSAT ozone products using satellite (GOME-2), ground-based (Brewer-Dobson, SAOZ, FTIR) and ozonesonde measurements, Atmospheric Measurement Techniques, 11, 5125–5152, https://doi.org/10.5194/amt-11-5125-2018, 2018.

Butchart, N.: The Brewer-Dobson circulation, Reviews of Geophysics, 52, 157–184, https://doi.org/https://doi.org/10.1002/2013RG000448, 2014.

Cadle, R. D., Fernald, F. G., and Frush, C. L.: Combined use of lidar and numerical diffusion models to estimate the quantity and dispersion of volcanic eruption clouds in the stratosphere: Vulcán Fuego, 1974, and Augustine, 1976, Journal of Geophysical Research (1896-1977), 82, 1783–1786, https://doi.org/https://doi.org/10.1029/JC082i012p01783, 1977.

Carr, J. L., Horváth, A., Wu, D. L., and Friberg, M. D.: Stereo Plume Height and Motion Retrievals for the Record-Setting Hunga Tonga-Hunga Ha'apai Eruption of 15 January 2022, Geophysical Research Letters, 49, e2022GL098131, https://doi.org/https://doi.org/10.1029/2022GL098131, e2022GL098131 2022GL098131, 2022.

Clarisse, L., Hurtmans, D., Clerbaux, C., Hadji-Lazaro, J., Ngadi, Y., and Coheur, P.-F.: Retrieval of sulphur dioxide from the infrared atmospheric sounding interferometer (IASI), Atmospheric Measurement Techniques, 5, 581–594, https://doi.org/10.5194/amt-5-581-2012, 2012.

Clarisse, L., Coheur, P.-F., Theys, N., Hurtmans, D., and Clerbaux, C.: The 2011 Nabro eruption, a SO_2 plume height analysis using IASI measurements, Atmospheric Chemistry and Physics, 14, 3095–3111, https://doi.org/10.5194/acp-14-3095-2014, 2014.

Clerbaux, C., Boynard, A., Clarisse, L., George, M., Hadji-Lazaro, J., Herbin, H., Hurtmans, D., Pommier, M., Razavi, A., Turquety, S., Wespes, C., and Coheur, P.-F.: Monitoring of atmospheric composition using the thermal infrared IASI/MetOp sounder, Atmospheric Chemistry and Physics, 9, 6041–6054, https://doi.org/10.5194/acp-9-6041-2009, 2009.

Coheur, P.-F., Clarisse, L., Turquety, S., Hurtmans, D., and Clerbaux, C.: IASI measurements of reactive trace species in biomass burning plumes, Atmospheric Chemistry and Physics, 9, 5655–5667, https://doi.org/10.5194/acp-9-5655-2009, 2009.

Crafford, T. C.: SO_2 emission of the 1974 eruption of Volcán Fuego, Guatemala, Bulletin Volcanologique, 39, 536–556, https://doi.org/10.1007/BF02596975, 1975.

Dhomse, S. S., Kinnison, D., Chipperfield, M. P., Salawitch, R. J., Cionni, I., Hegglin, M. I., Abraham, N. L., Akiyoshi, H., Archibald, A. T., Bednarz, E. M., Bekki, S., Braesicke, P., Butchart, N., Dameris, M., Deushi, M., Frith, S., Hardiman, S. C., Hassler, B., Horowitz, L. W., Hu, R.-M., Jöckel, P., Josse, B., Kirner, O., Kremser, S., Langematz, U., Lewis, J., Marchand, M., Lin, M., Mancini, E., Marécal, V., Michou, M., Morgenstern, O., O'Connor, F. M., Oman, L., Pitari, G., Plummer, D. A., Pyle, J. A., Revell, L. E., Rozanov, E., Schofield, R., Stenke, A., Stone, K., Sudo, K., Tilmes, S., Visioni, D., Yamashita, Y., and Zeng, G.: Estimates of ozone return dates from Chemistry-Climate Model Initiative simulations, Atmospheric Chemistry and Physics, 18, 8409–8438, https://doi.org/10.5194/acp-18-8409-2018, 2018.

Doiron, S. D., Bluth, G. J. S., Schnetzler, C. C., Krueger, A. J., and Walter, L. S.: Transport of Cerro Hudson SO2 clouds, Eos, Transactions American Geophysical Union, 72, 489–498, https://doi.org/https://doi.org/10.1029/90EO00354, 1991.

Draxler, R. and Hess, G.: Description of the HYSPLIT_4 modelling system, NOAA Tech. Mem. ERL ARL-224, 1997.

Draxler, R. and Hess, G.: An overview of the HYSPLIT_4 modelling system for trajectories, dispersion, and deposition, Australian Meteorological Magazine, 47, 295–308, 1998.

Duflot, V., Bègue, N., Pouliquen, M.-L., Goloub, P., and Metzger, J.-M.: Aerosols on the Tropical Island of La Réunion (21°S, 55°E): Assessment of Climatology, Origin of Variability and Trend, Remote Sensing, 14, 4945, https://doi.org/10.3390/rs14194945, 2022.

Evan, S., Brioude, J., Rosenlof, K. H., Gao, R.-S., Portmann, R. W., Zhu, Y., Volkamer, R., Lee, C. F., Metzger, J.-M., Lamy, K., Walter, P., Alvarez, S. L., Flynn, J. H., Asher, E., Todt, M., Davis, S. M., Thornberry, T., Vömel, H., Wienhold, F. G., Stauffer, R. M., Millán, L., Santee, M. L., Froidevaux, L., and Read, W. G.: Rapid ozone depletion after humidification of the stratosphere by the Hunga Tonga Eruption, Science, 382, eadg2551, https://doi.org/10.1126/science.adg2551, 2023.

Giles, D. M., Sinyuk, A., Sorokin, M. G., Schafer, J. S., Smirnov, A., Slutsker, I., Eck, T. F., Holben, B. N., Lewis, J. R., Campbell, J. R., Welton, E. J., Korkin, S. V., and Lyapustin, A. I.: Advancements in the Aerosol Robotic Network (AERONET) Version 3 database

– automated near-real-time quality control algorithm with improved cloud screening for Sun photometer aerosol optical depth (AOD) measurements, Atmospheric Measurement Techniques, 12, 169–209, https://doi.org/10.5194/amt-12-169-2019, 2019.

Gobbi, G. P., Congeduti, F., and Adriani, A.: Early stratospheric effects of the Pinatubo Eruption, Geophysical Research Letters, 19, 997–1000, https://doi.org/https://doi.org/10.1029/92GL01038, 1992.

550   Godin, S., Carswell, A. I., Donovan, D. P., Claude, H., Steinbrecht, W., McDermid, I. S., McGee, T. J., Gross, M. R., Nakane, H., Swart, D. P. J., Bergwerff, H. B., Uchino, O., von der Gathen, P., and Neuber, R.: Ozone differential absorption lidar algorithm intercomparison, Appl. Opt., 38, 6225–6236, https://doi.org/10.1364/AO.38.006225, 1999.

Godin-Beekmann, S., Porteneuve, J., and Garnier, A.: Systematic DIAL lidar monitoring of the stratospheric ozone vertical distribution at Observatoire de Haute-Provence (43.92 N, 5.71 E), Journal of environmental Monitoring, 5, 57–67, 2003.

555   Guo, S., Bluth, G. J. S., Rose, W. I., Watson, I. M., and Prata, A. J.: Re-evaluation of SO2 release of the 15 June 1991 Pinatubo eruption using ultraviolet and infrared satellite sensors, Geochemistry, Geophysics, Geosystems, 5, https://doi.org/https://doi.org/10.1029/2003GC000654, 2004.

Hofmann, D. J. and Oltmans, S. J.: Anomalous Antarctic ozone during 1992: Evidence for Pinatubo volcanic aerosol effects, Journal of Geophysical Research: Atmospheres, 98, 18 555–18 561, https://doi.org/https://doi.org/10.1029/93JD02092, 1993.

560   Hofmann, D. J. and Solomon, S.: Ozone destruction through heterogeneous chemistry following the eruption of El Chichón, Journal of Geophysical Research: Atmospheres, 94, 5029–5041, https://doi.org/https://doi.org/10.1029/JD094iD04p05029, 1989.

Hurtmans, D., Coheur, P.-F., Wespes, C., Clarisse, L., Scharf, O., Clerbaux, C., Hadji-Lazaro, J., George, M., and Turquety, S.: FORLI radiative transfer and retrieval code for IASI, Journal of Quantitative Spectroscopy and Radiative Transfer, 113, 1391–1408, https://doi.org/https://doi.org/10.1016/j.jqsrt.2012.02.036, three Leaders in Spectroscopy, 2012.

565   IPCC: Climate Change 2013: The Physical Science Basis. Contribution of Working Group I to the Fifth Assessment Report of the Intergovernmental Panel on Climate Change, in: Cambridge University Press, https://www.ipcc.ch/report/ar5/wg1/, 2013.

IPCC: Climate Change 2021: The Physical Science Basis. Contribution of Working Group I to the Sixth Assessment Report of the Intergovernmental Panel on Climate Change, in: Cambridge University Press, https://www.ipcc.ch/report/ar6/wg1/, 2021.

Ivatt, P. D., Evans, M. J., and Lewis, A. C.: Suppression of surface ozone by an aerosol-inhibited photochemical ozone regime, Nature

570   Geoscience, 15, 536–540, https://doi.org/10.1038/s41561-022-00972-9, 2022.

Ivy, D. J., Solomon, S., Kinnison, D., Mills, M. J., Schmidt, A., and Neely III, R. R.: The influence of the Calbuco eruption on the 2015 Antarctic ozone hole in a fully coupled chemistry-climate model, Geophysical Research Letters, 44, 2556–2561, https://doi.org/https://doi.org/10.1002/2016GL071925, 2017.

Jacob, D. J.: Introduction to atmospheric chemistry, Princeton University Press, 1999.

575   Khaykin, S., Podglajen, A., Ploeger, F., Grooß, J.-U., Tence, F., Bekki, S., Khlopenkov, K., Bedka, K., Rieger, L., Baron, A., Godin-Beekmann, S., Legras, B., Sellitto, P., Sakai, T., Barnes, J., Uchino, O., Morino, I., Nagai, T., Wing, R., Baumgarten, G., Gerding, M., Duflot, V., Payen, G., Jumelet, J., Querel, R., Liley, B., Bourassa, A., Clouser, B., Feofilov, A., Hauchecorne, A., and Ravetta, F.: Global perturbation of stratospheric water and aerosol burden by Hunga eruption, Communications Earth & Environment, 3, 316, https://doi.org/10.1038/s43247-022-00652-x, 2022.

580   Kirchner, I., Stenchikov, G. L., Graf, H.-F., Robock, A., and Antuña, J. C.: Climate model simulation of winter warming and summer cooling following the 1991 Mount Pinatubo volcanic eruption, Journal of Geophysical Research: Atmospheres, 104, 19 039–19 055, https://doi.org/https://doi.org/10.1029/1999JD900213, 1999.

Kremser, S., Thomason, L. W., von Hobe, M., Hermann, M., Deshler, T., Timmreck, C., Toohey, M., Stenke, A., Schwarz, J. P., Weigel, R., Fueglistaler, S., Prata, F. J., Vernier, J.-P., Schlager, H., Barnes, J. E., Antuña-Marrero, J.-C., Fairlie, D., Palm, M., Mahieu, E., Notholt, J., Rex, M., Bingen, C., Vanhellemont, F., Bourassa, A., Plane, J. M. C., Klocke, D., Carn, S. A., Clarisse, L., Trickl, T., Neely, R., James, A. D., Rieger, L., Wilson, J. C., and Meland, B.: Stratospheric aerosol—Observations, processes, and impact on climate, Reviews of Geophysics, 54, 278–335, https://doi.org/https://doi.org/10.1002/2015RG000511, 2016.

Legras, B., Duchamp, C., Sellitto, P., Podglajen, A., Carboni, E., Siddans, R., Grooß, J.-U., Khaykin, S., and Ploeger, F.: The evolution and dynamics of the Hunga Tonga–Hunga Ha'apai sulfate aerosol plume in the stratosphere, Atmospheric Chemistry and Physics, 22, 14 957–14 970, https://doi.org/10.5194/acp-22-14957-2022, 2022.

Livesey, N. J., Read, W. G., Wagner, P. A., Froidevaux, L., Lambert, A., Manney, G. L., Valle, L. F. M., Pumphrey, H. C., Santee, M. L., Schwartz, M. J., Wang, S., Fuller, R. A., Jarnot, R. F., Knosp, B. W., Martinez, E., and Lay, R. R.: Version 4.2x Level 2 and 3 data quality and description document., https://mls.jpl.nasa.gov/data/v4-2_data_quality_document.pdf, 2020.

Livesey, N. J., Read, W. G., Wagner, P. A., Froidevaux, L., Santee, M. L., Schwartz, M. J., Lambert, A., Valle, L. F. M., Pumphrey, H. C., Manney, G. L., Fuller, R. A., Jarnot, R. F., Knosp, B. W., and Lay, R. R.: Version 5.0x Level 2 and 3 data quality and description document., https://mls.jpl.nasa.gov/data/v5-0_data_quality_document.pdf, 2022.

Matsumura, Y. and Ananthaswamy, H. N.: Toxic effects of ultraviolet radiation on the skin, Toxicology and Applied Pharmacology, 195, 298–308, https://doi.org/https://doi.org/10.1016/j.taap.2003.08.019, toxicology of the Skin, 2004.

McCormick, M., Thomason, L., and Trepte, C.: Atmospheric effects of the Mt Pinatubo eruption, Nature, 373, 399–404, https://www.nature.com/articles/373399a0, 1995.

Mills, G., Sharps, K., Simpson, D., Pleijel, H., Frei, M., Burkey, K., Emberson, L., Uddling, J., Broberg, M., Feng, Z., Kobayashi, K., and Agrawal, M.: Closing the global ozone yield gap: Quantification and cobenefits for multistress tolerance, Global Change Biology, 24, 4869–4893, https://doi.org/https://doi.org/10.1111/gcb.14381, 2018.

Millán, L., Santee, M. L., Lambert, A., Livesey, N. J., Werner, F., Schwartz, M. J., Pumphrey, H. C., Manney, G. L., Wang, Y., Su, H., Wu, L., Read, W. G., and Froidevaux, L.: The Hunga Tonga-Hunga Ha'apai Hydration of the Stratosphere, Geophysical Research Letters, 49, e2022GL099 381, https://doi.org/https://doi.org/10.1029/2022GL099381, e2022GL099381 2022GL099381, 2022.

Molina, M. J. and Rowland, F. S.: Stratospheric sink for chlorofluoromethanes: chlorine atom-catalysed destruction of ozone, Nature, 249, 810–812, https://doi.org/10.1038/249810a0, 1974.

National Oceanic and Atmospheric Administration (NOAA): Global Data Assimilation System (GDAS), https://www.ready.noaa.gov/data/archives/gdas1/, accessed September 2022, 2023.

Neale, R. E., Barnes, P. W., Robson, T. M., Neale, P. J., Williamson, C. E., Zepp, R. G., Wilson, S. R., Madronich, S., Andrady, A. L., Heikkilä, A. M., Bernhard, G. H., Bais, A. F., Aucamp, P. J., Banaszak, A. T., Bornman, J. F., Bruckman, L. S., Byrne, S. N., Foereid, B., Häder, D.-P., Hollestein, L. M., Hou, W.-C., Hylander, S., Jansen, M. A. K., Klekociuk, A. R., Liley, J. B., Longstreth, J., Lucas, R. M., Martinez-Abaigar, J., McNeill, K., Olsen, C. M., Pandey, K. K., Rhodes, L. E., Robinson, S. A., Rose, K. C., Schikowski, T., Solomon, K. R., Sulzberger, B., Ukpebor, J. E., Wang, Q.-W., Wängberg, S.-Å., White, C. C., Yazar, S., Young, A. R., Young, P. J., Zhu, L., and Zhu, M.: Environmental effects of stratospheric ozone depletion, UV radiation, and interactions with climate change: UNEP Environmental Effects Assessment Panel, Update 2020, Photochemical & Photobiological Sciences, 20, 1–67, https://doi.org/10.1007/s43630-020-00001-x, 2021.

Nuvolone, D., Petri, D., and Voller, F.: The Effects of Ozone on Human Health, Environmental Science and Pollution Research, 25, 8074–8088, https://doi.org/10.1007/s11356-017-9239-3, 2018.

Orphal, J., Staehelin, J., Tamminen, J., Braathen, G., De Backer, M.-R., Bais, A., Balis, D., Barbe, A., Bhartia, P. K., Birk, M., Burkholder, J. B., Chance, K., von Clarmann, T., Cox, A., Degenstein, D., Evans, R., Flaud, J.-M., Flittner, D., Godin-Beekmann, S., Gorshelev, V., Gratien, A., Hare, E., Janssen, C., Kyrölä, E., McElroy, T., McPeters, R., Pastel, M., Petersen, M., Petropavlovskikh, I., Picquet-Varrault, B., Pitts, M., Labow, G., Rotger-Languereau, M., Leblanc, T., Lerot, C., Liu, X., Moussay, P., Redondas, A., Van Roozendael, M., Sander, S. P., Schneider, M., Serdyuchenko, A., Veefkind, P., Viallon, J., Viatte, C., Wagner, G., Weber, M., Wielgosz, R. I., and Zehner, C.: Absorption cross-sections of ozone in the ultraviolet and visible spectral regions: Status report 2015, Journal of Molecular Spectroscopy, 327, 105–121, https://doi.org/https://doi.org/10.1016/j.jms.2016.07.007, new Visions of Spectroscopic Databases, Volume II, 2016.

Pazmiño, A.: DIAL lidar for ozone measurements, in: Journal de Physique IV (Proceedings), vol. 139, pp. 361–372, EDP sciences, 2006.

Pitts, D. G., Cullen, A. P., and Hacker, P. D.: Ocular effects of ultraviolet radiation from 295 to 365 nm., Investigative Ophthalmology & Visual Science, 16, 932–939, 1977.

Plumb, R. A. and Eluszkiewicz, J.: The Brewer–Dobson Circulation: Dynamics of the Tropical Upwelling, Journal of the Atmospheric Sciences, 56, 868 – 890, https://doi.org/https://doi.org/10.1175/1520-0469(1999)056<0868:TBDCDO>2.0.CO;2, 1999.

Pommereau, J. P. and Goutail, F.: O_3 and NO_2 ground-based measurements by visible spectrometry during Arctic winter and spring 1988, Geophysical Research Letters, 15, 891–894, https://doi.org/10.1029/GL015i008p00891, 1988.

Portafaix, T., Godin-Beekmann, S., Payen, G., Langerock, B., Fernandez, S., Posny, F., Cammas, J.-P., Metzger, J.-M., Bencherif, H., Vigouroux, C., and Marquestaut, N.: Ozone profiles obtained by DIAL technique at Maïdo Observatory in La Réunion Island: comparisons with ECC ozone-sondes, ground-based FTIR spectrometer and microwave radiometer measurements, EPJ Web of Conferences, 119, https://doi.org/10.1051/epjconf/201611905005, 2015.

Ramaswamy, V., Schwarzkopf, M. D., Randel, W. J., Santer, B. D., Soden, B. J., and Stenchikov, G. L.: Anthropogenic and Natural Influences in the Evolution of Lower Stratospheric Cooling, Science, 311, 1138–1141, https://doi.org/10.1126/science.1122587, 2006.

Robock, A.: Volcanic eruptions and climate, Reviews of Geophysics, 38, 191–219, https://doi.org/https://doi.org/10.1029/1998RG000054, 2000.

Rowland, F. S.: Stratospheric ozone depletion by chlorofluorocarbons (Nobel lecture), Angewandte Chemie International Edition in English, 35, 1786–1798, 1996.

Schoeberl, M. R., Doiron, S. D., Lait, L. R., Newman, P. A., and Krueger, A. J.: A simulation of the Cerro Hudson SO2 cloud, Journal of Geophysical Research: Atmospheres, 98, 2949–2955, https://doi.org/https://doi.org/10.1029/92JD02517, 1993.

Sellitto, P., Podglajen, A., Belhadji, R., Boichu, M., Carboni, E., Cuesta, J., Duchamp, C., Kloss, C., Siddans, R., Bègue, N., Blarel, L., Jegou, F., Khaykin, S., Renard, J.-B., and Legras, B.: The unexpected radiative impact of the Hunga Tonga eruption of 15th January 2022, Communications Earth & Environment, 3, 288, https://doi.org/10.1038/s43247-022-00618-z, 2022.

Sicard, M., Baron, A. A., Ranaivombola, M., Gantois, D., Millet, T., Sellitto, P., Bègue, N., Bencherif, H., Payen, G., Marquestaut, N., and Duflot, V.: Radiative impact of the Hunga stratospheric volcanic plume: role of aerosols and water vapor over Reunion Island (21º S, 55º E), Atmospheric Chemistry and Physics, 2024.

Solomon, S.: The mystery of the Antarctic ozone "hole", Reviews of Geophysics, 26, 131–148, 1988.

Solomon, S.: Stratospheric ozone depletion: A review of concepts and history, Reviews of Geophysics, 37, 275–316, https://doi.org/https://doi.org/10.1029/1999RG900008, 1999.

Stenchikov, G. L., Kirchner, I., Robock, A., Graf, H.-F., Antuña, J. C., Grainger, R. G., Lambert, A., and Thomason, L.: Radiative forcing from the 1991 Mount Pinatubo volcanic eruption, Journal of Geophysical Research: Atmospheres, 103, 13 837–13 857, https://doi.org/https://doi.org/10.1029/98JD00693, 1998.

Taha, G., Loughman, R., Zhu, T., Thomason, L., Kar, J., Rieger, L., and Bourassa, A.: OMPS LP Version 2.0 multi-wavelength aerosol extinction coefficient retrieval algorithm, Atmospheric Measurement Techniques, 14, 1015–1036, https://doi.org/10.5194/amt-14-1015-2021, 2021.

Taha, G., Loughman, R., Colarco, P. R., Zhu, T., Thomason, L. W., and Jaross, G.: Tracking the 2022 Hunga Tonga-Hunga Ha'apai Aerosol Cloud in the Upper and Middle Stratosphere Using Space-Based Observations, Geophysical Research Letters, 49, e2022GL100 091, https://doi.org/https://doi.org/10.1029/2022GL100091, e2022GL100091 2022GL100091, 2022.

Tie, X. and Brasseur, G.: The response of stratospheric ozone to volcanic eruptions: Sensitivity to atmospheric chlorine loading, Geophysical Research Letters, 22, 3035–3038, https://doi.org/https://doi.org/10.1029/95GL03057, 1995.

Vömel, H., Evan, S., and Tully, M.: Water vapor injection into the stratosphere by Hunga Tonga-Hunga Ha'apai, Science, 377, 1444–1447, https://doi.org/10.1126/science.abq2299, 2022.

Waters, J., Froidevaux, L., Harwood, R., Jarnot, R., Pickett, H., Read, W., Siegel, P., Cofield, R., Filipiak, M., Flower, D., Holden, J., Lau, G., Livesey, N., Manney, G., Pumphrey, H., Santee, M., Wu, D., Cuddy, D., Lay, R., Loo, M., Perun, V., Schwartz, M., Stek, P., Thurstans, R., Boyles, M., Chandra, K., Chavez, M., Chen, G.-S., Chudasama, B., Dodge, R., Fuller, R., Girard, M., Jiang, J., Jiang, Y., Knosp, B., LaBelle, R., Lam, J., Lee, K., Miller, D., Oswald, J., Patel, N., Pukala, D., Quintero, O., Scaff, D., Van Snyder, W., Tope, M., Wagner, P., and Walch, M.: The Earth observing system microwave limb sounder (EOS MLS) on the aura Satellite, IEEE Transactions on Geoscience and Remote Sensing, 44, 1075–1092, https://doi.org/10.1109/TGRS.2006.873771, 2006.

Weber, M., Dikty, S., Burrows, J. P., Garny, H., Dameris, M., Kubin, A., Abalichin, J., and Langematz, U.: The Brewer-Dobson circulation and total ozone from seasonal to decadal time scales, Atmospheric Chemistry and Physics, 11, 11 221–11 235, https://doi.org/10.5194/acp-11-11221-2011, 2011.

WMO: Scientific assessment of ozone depletion: 1998, Global ozone research and monitoring project-report no. 44, World Meteorological Organization, Geneva, Switzerland, https://library.wmo.int/idurl/4/50254, 1999.

WMO: Scientific assessment of ozone depletion: 2018, Gaw report no. 278, World Meteorological Organization, Geneva, Switzerland, https://library.wmo.int/idurl/4/58360, 2022.

Wright, C. J., Hindley, N. P., Alexander, M. J., Barlow, M., Hoffmann, L., Mitchell, C. N., Prata, F., Bouillon, M., Carstens, J., Clerbaux, C., Osprey, S. M., Powell, N., Randall, C. E., and Yue, J.: Surface-to-space atmospheric waves from Hunga Tonga–Hunga Ha'apai eruption, Nature, 609, 741–746, https://doi.org/10.1038/s41586-022-05012-5, 2022.

Yook, S., Thompson, D. W. J., and Solomon, S.: Climate Impacts and Potential Drivers of the Unprecedented Antarctic Ozone Holes of 2020 and 2021, Geophysical Research Letters, 49, e2022GL098 064, https://doi.org/https://doi.org/10.1029/2022GL098064, e2022GL098064 2022GL098064, 2022.

Zhu, Y., Toon, O. B., Kinnison, D., Harvey, V. L., Mills, M. J., Bardeen, C. G., Pitts, M., Bègue, N., Renard, J.-B., Berthet, G., and Jégou, F.: Stratospheric Aerosols, Polar Stratospheric Clouds, and Polar Ozone Depletion After the Mount Calbuco Eruption in 2015, Journal of Geophysical Research: Atmospheres, 123, 12,308–12,331, https://doi.org/https://doi.org/10.1029/2018JD028974, 2018.

Zhu, Y., Portmann, R. W., Kinnison, D., Toon, O. B., Millán, L., Zhang, J., Vömel, H., Tilmes, S., Bardeen, C. G., Wang, X., Evan, S., Randel, W. J., and Rosenlof, K. H.: Stratospheric ozone depletion inside the volcanic plume shortly after the 2022 Hunga Tonga eruption, Atmospheric Chemistry and Physics, 23, 13 355–13 367, https://doi.org/10.5194/acp-23-13355-2023, 2023.

Zuo, M., Zhou, T., Man, W., Chen, X., Liu, J., Liu, F., and Gao, C.: Volcanoes and Climate: Sizing up the Impact of the Recent Hunga Tonga-Hunga Ha'apai Volcanic Eruption from a Historical Perspective, Advances in Atmospheric Sciences, https://doi.org/10.1007/s00376-022-2034-1, 2022.
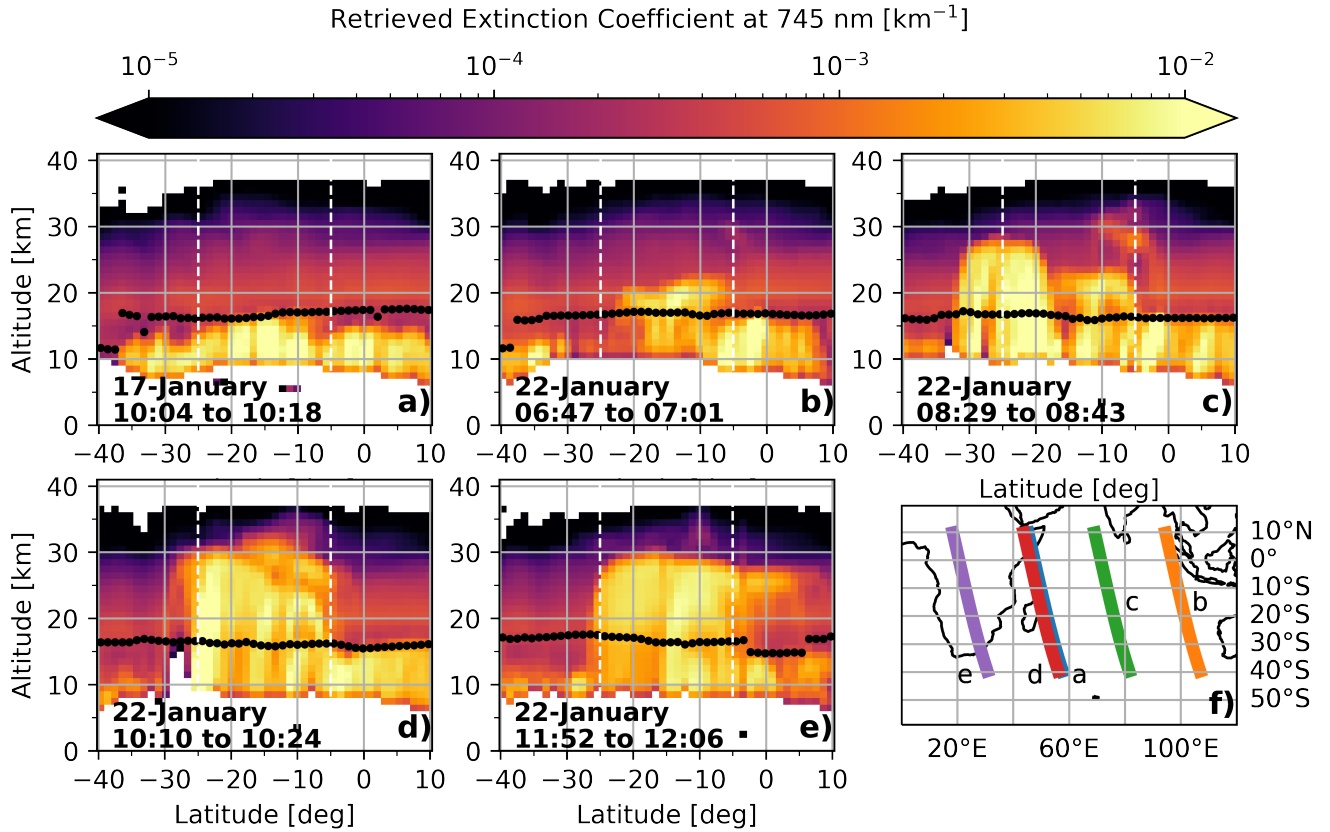
Figure 1. OMPS-LP aerosol extinction height-latitude cross-sections over the Indian Ocean at 745 nm for **a**) background conditions on 17 January prior to the passage of the volcanic plume and **b–e**) during the passage of the plume on 22 January. Panel **f**) shows the satellite track corresponding to each overpass. The superimposed black dots on panels **a–e**) indicate the instrument's estimation of the tropopause height. Vertical dashed lines mark the positions of the 5° S and 25° S latitude lines.
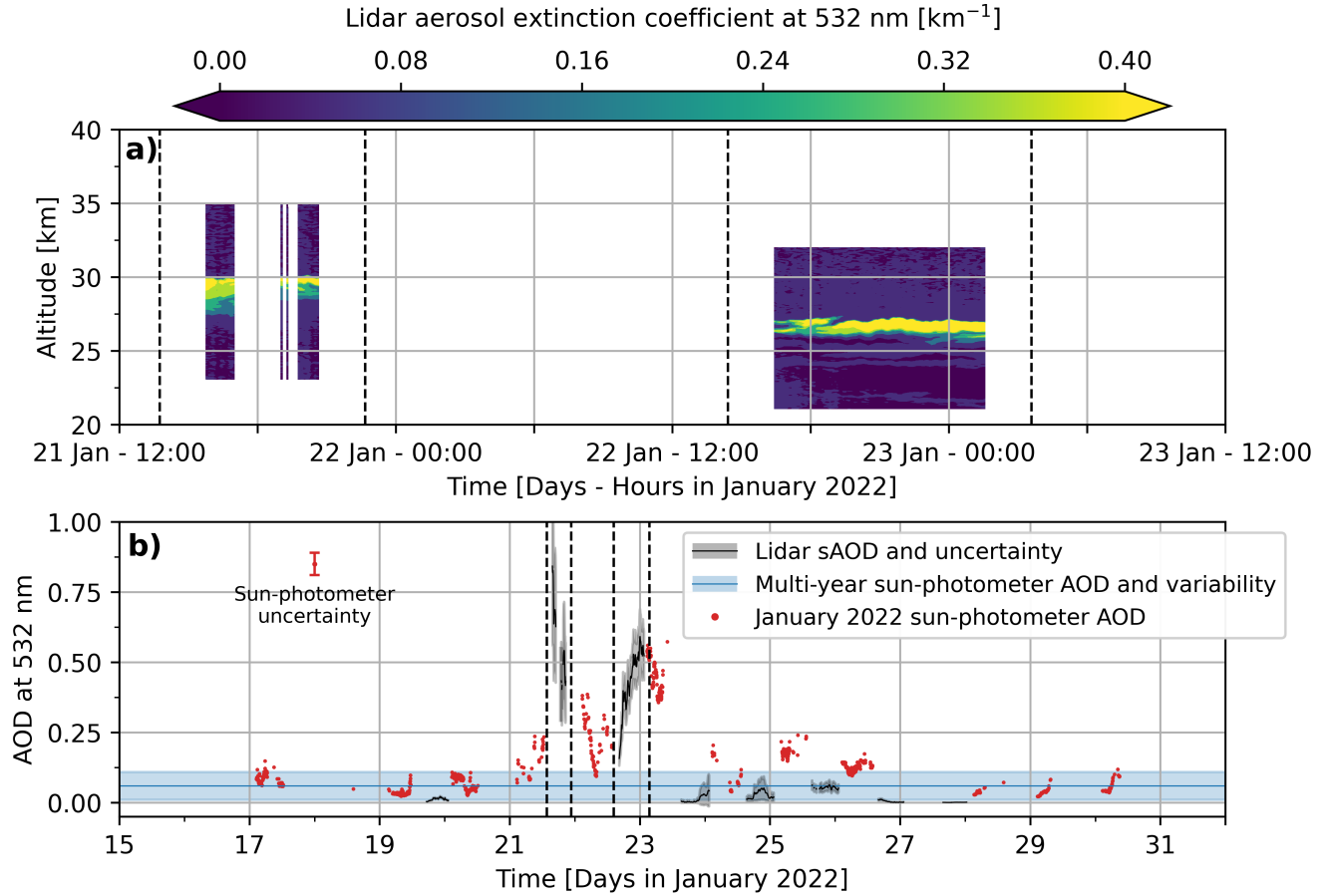
Figure 2. Aerosol lidar extinction profiles at 532 nm (**a**) and aerosol lidar sAOD in black with level 2.0 sun-photometer total AOD in red (**b**). The gray shading indicates the lidar sAOD uncertainty, while the sun-photometer total AOD uncertainty is illustrated in the upper part of panel **b**). The blue line and shaded area represent average and standard deviation values given by level 2.0 sun-photometer data from the months of January taken between 2003 to 2021. The common observation periods in the two panels are visually represented with vertical dashed lines.
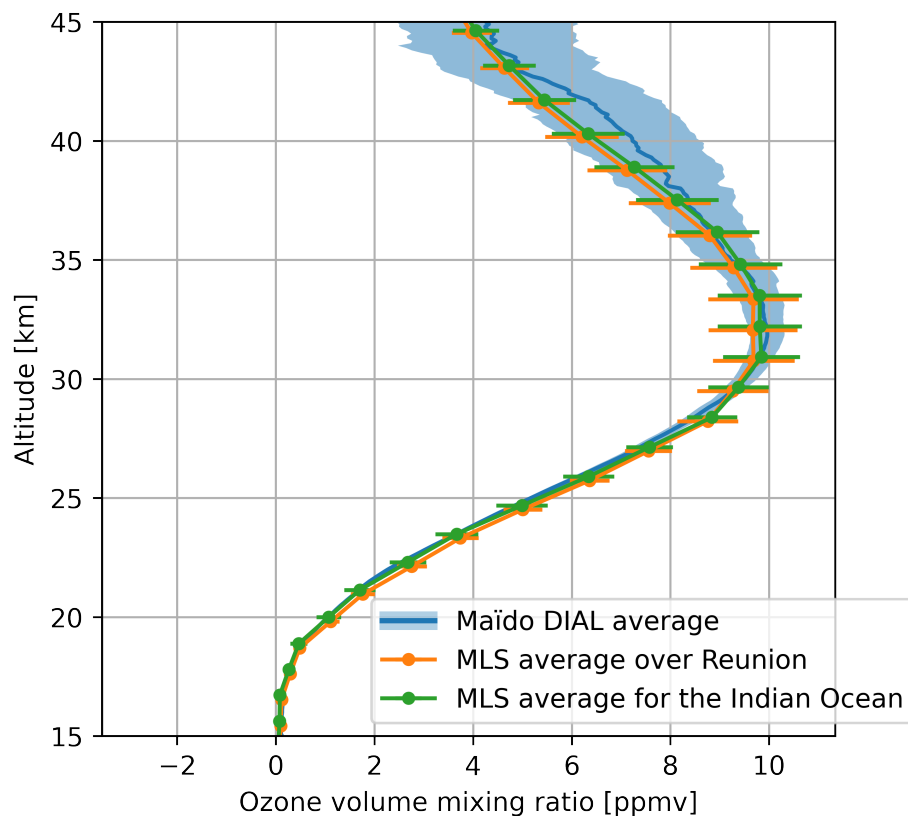
Figure 3. Average January stratospheric DIAL profile from 2013—2021 observations at Reunion (blue), alongside average January MLS profiles for Reunion (orange) and the full study region (green). Standard deviations are shown as a shaded region for the DIAL profile and as horizontal bars for the MLS profiles.
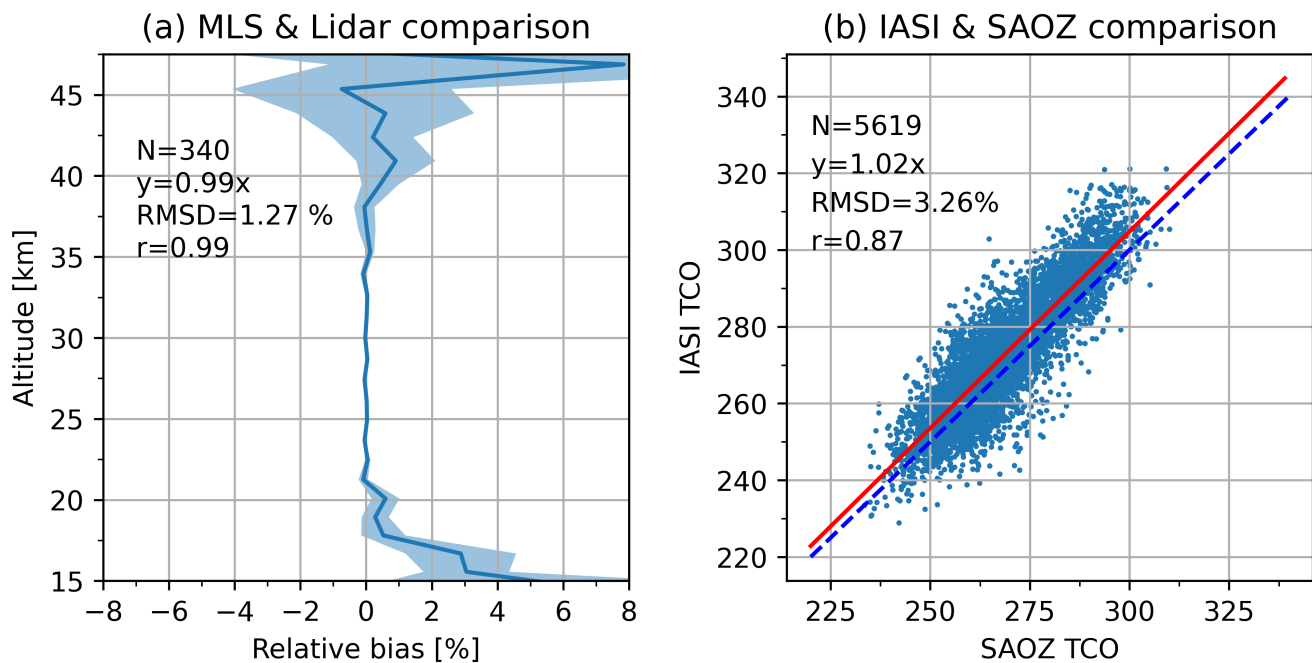
Figure 4. a) Mean relative bias (solid line) and standard error (shaded area) comparing nocturnal DIAL ozone profiles to the corresponding daily MLS v5 ozone profiles between January 2013 and December 2021. **b**) Direct comparison between SAOZ TCO and IASI TCO from data points obtained between March 2013 and December 2021. Statistical results presented in the left side each of panel were obtained from the comparison of all data points, irrespective of the altitude level, date and time of day.
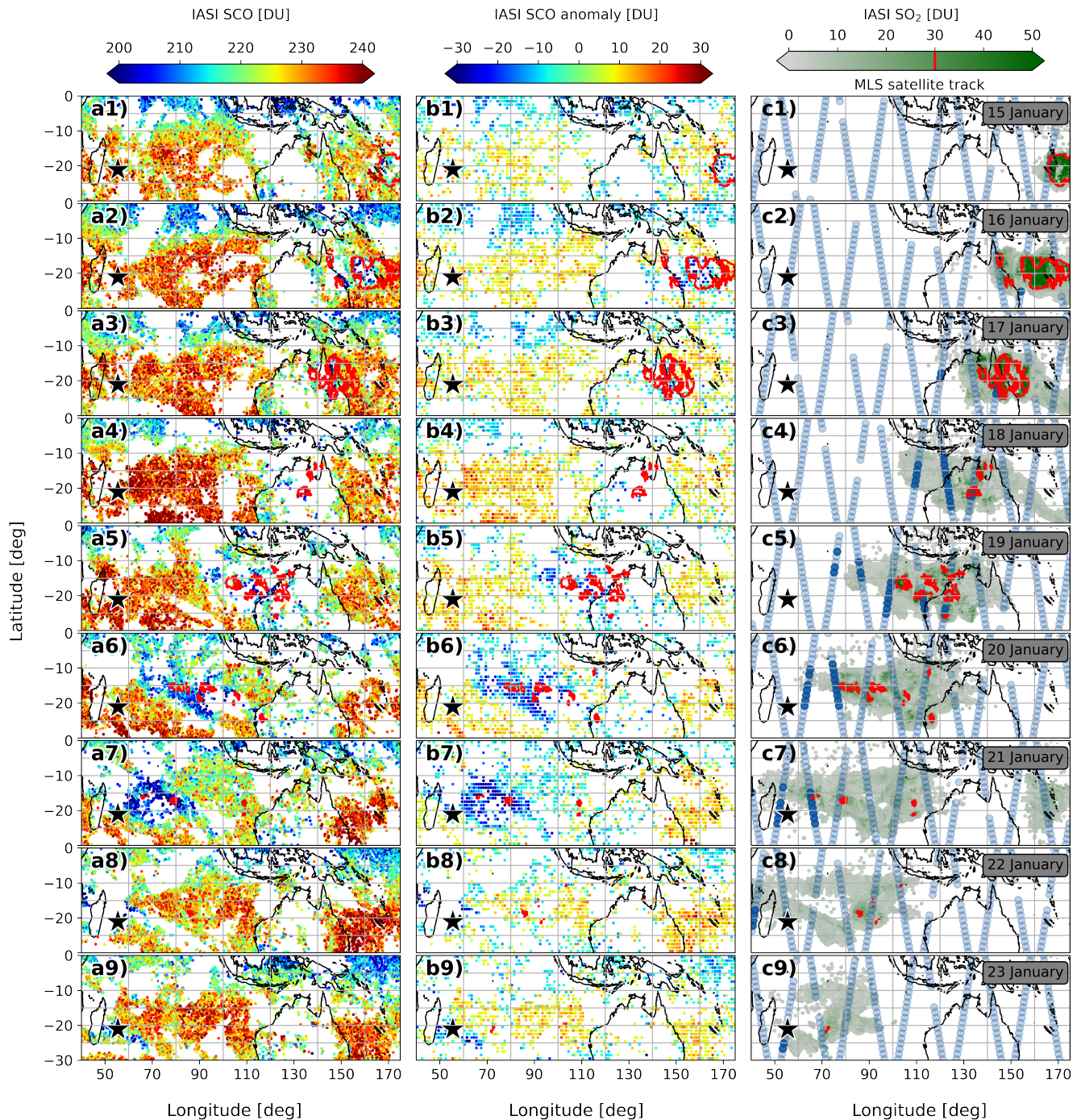
Figure 5. Daily evolution of SCO (**a1-a9**) and SCO significant anomaly at 2σ (**b1-b9**) observed by IASI alongside the satellite track of MLS (blue dots) and total SO_2 column from IASI (**c1-c9**) between 15 and 23 January. Dark blue dots on the MLS track represent the location of profiles meeting the selection criterion. The red contour indicates the regions where total SO_2 column is greater than 30 DU. The black and white star represents the location of Reunion. Each row corresponds to a distinct day, and the date of observation is indicated for each row in the right column.
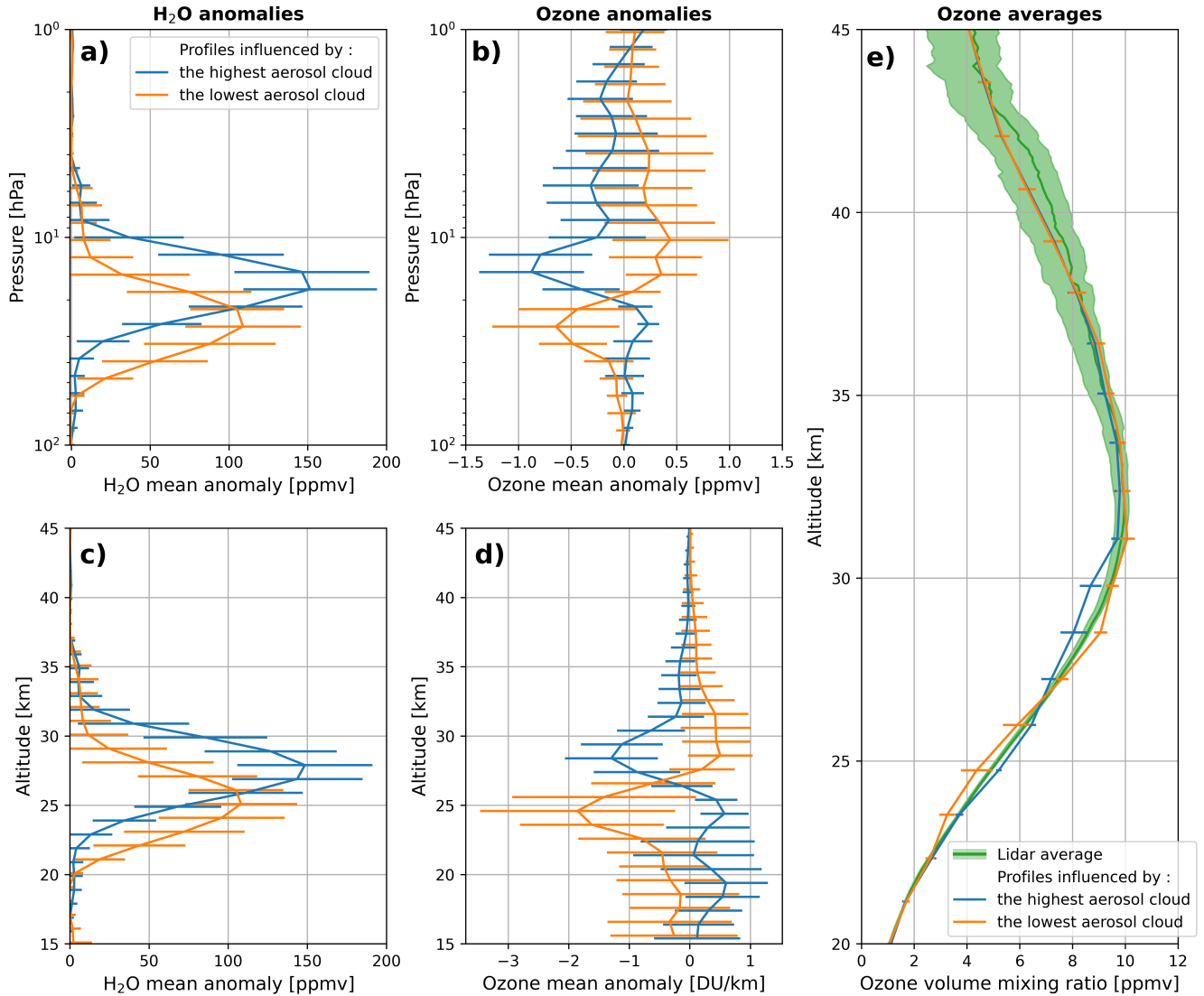
26

Figure 6. Mean anomalies and $\pm 1\sigma$ standard deviation (horizontal bars) in **a-c**) water vapor and **b-d**) ozone from v4 MLS profiles that met the selection criterion. The upper row (panels **a-b**) presents measurements from raw profiles in volume mixing ratio over a pressure range, while the lower row (panels **c-d**) shows the same data over an altitude range, with ozone expressed in DU/km. Panel **e**) displays the January mean lidar ozone profile with its $\pm 2\sigma$ standard deviation and the average v4 MLS ozone profiles influenced by one of the aerosol clouds with the corresponding $\pm 1\sigma$ standard deviation. Profiles influenced by the highest and lowest sulfate aerosol clouds are displayed in blue and orange, respectively.
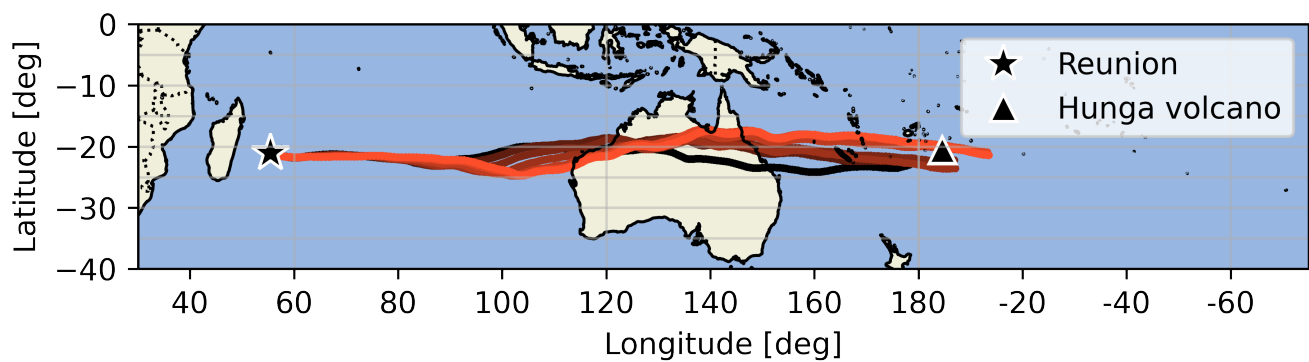
Figure 7. HYSPLIT back trajectories of 240 hours ending on 21 January at 00:00 UTC at the location of Saint-Denis, Reunion, between 23.5 and 29.0 km height. The star and triangle symbols indicate the ending point and the Hunga volcano location, respectively. The back trajectories are displayed with a color gradient, ranging from black for the 23.5 km to orange for 29.0 km.
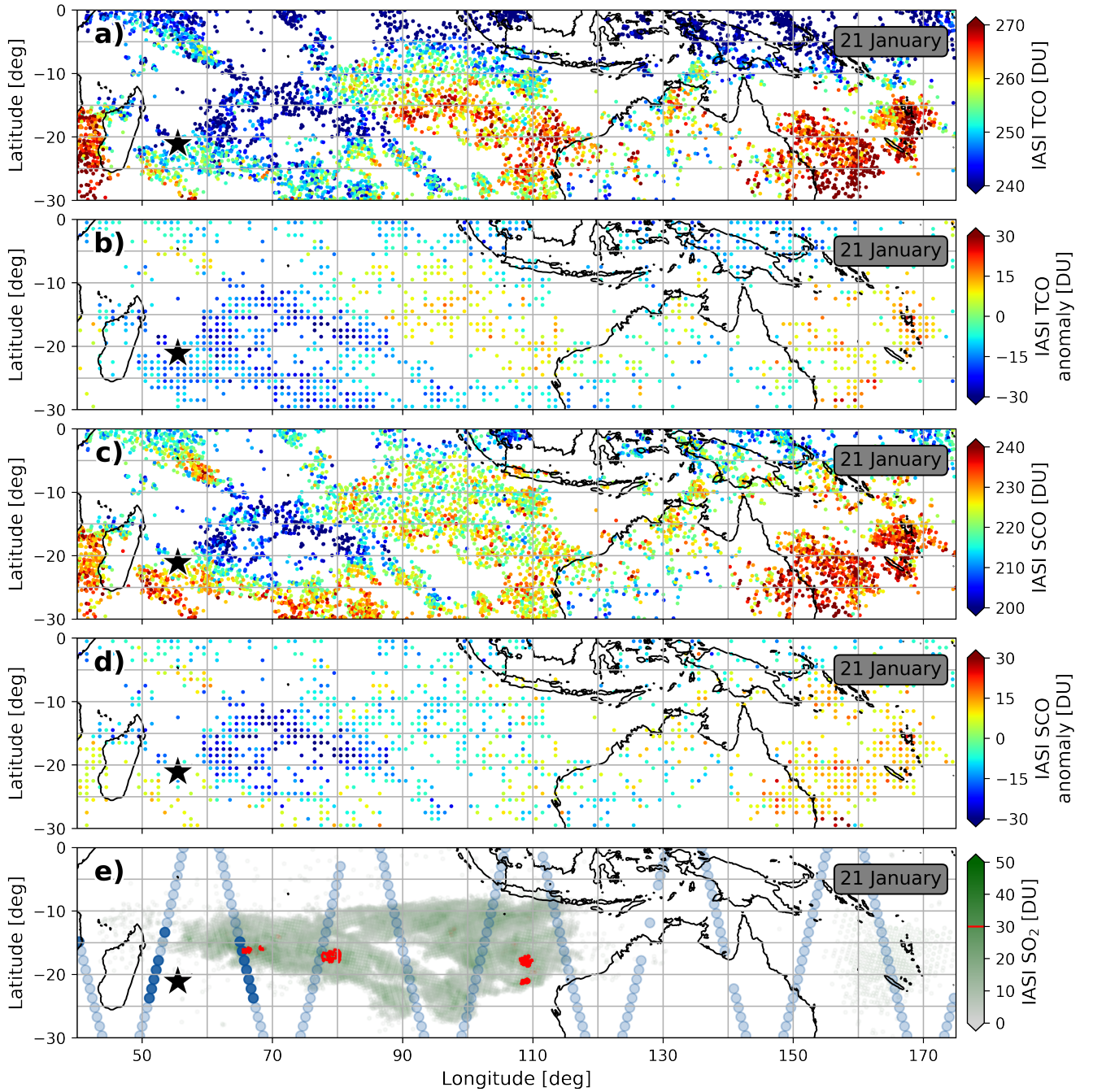
Figure A1. IASI TCO (**a**), TCO anomaly (**b**), SCO (**c**) and SCO anomaly (**d**) alongside the satellite track of MLS (blue dots) and IASI total SO$_2$ column (**e**) for 21 January when the depletion event passes over Reunion. Dark blue dots on the MLS track represent the location of profiles meeting the selection criterion. Anomalies shown in panels **b**) and **d**) are significant at the 2σ level. The red contour indicates the regions where total SO$_2$ column is greater than 30 DU, and the black and white star represents the location of Reunion.